Damped Lyα absorbers in star-forming galaxies at z < 0.15 detected with the Hubble Space Telescope and implications for galactic evolution

Kulkarni, V.P.; Bowen, D.V.; Straka, L.A.; York, D.G.; Gupta, N.; Noterdaeme, P.; Srianand, R.

Damped Lyα Absorbers in Star-forming Galaxies at $z < 0.15$ Detected with the Hubble Space Telescope and Implications for Galactic Evolution

Varsha P. Kulkarni[1] , David V. Bowen[2] , Lorrie A. Straka[3] , Donald G. York[4,8] , Neeraj Gupta[5] ,
Pasquier Noterdaeme[6,7] , and Raghunathan Srianand[5]
[1] Department of Physics & Astronomy, University of South Carolina, Columbia, SC 29208, USA; kulkarni@sc.edu
[2] Department of Astrophysical Sciences, Princeton University, Princeton, NJ 08544, USA
[3] Sterrewacht Leiden, Leiden University, PO Box 9513, NL-2300 R.A. Leiden, The Netherlands
[4] Department of Astronomy & Astrophysics, University of Chicago, Chicago, IL 60637, USA
[5] Inter-University Centre for Astronomy and Astrophysics, Post Bag 4, Ganeshkhind 411007, Pune, India
[6] Institut d'Astrophysique de Paris, UMR7095, CNRS-UMPC, 98bis bd Arago, 75014 Paris, France
[7] Franco-Chilean Laboratory for Astronomy, IRL 3386, CNRS and Departamento de Astronomía, Universidad de Chile, Casilla 36-D, Santiago, Chile

Abstract

We report Hubble Space Telescope Cosmic Origins Spectrograph spectroscopy of 10 quasars with foreground star-forming galaxies at $0.02 < z < 0.14$ within impact parameters of $\sim$1–7 kpc. We detect damped/sub-damped Lyα (DLA/sub-DLA) absorption in 100% of cases where no higher-redshift Lyman-limit systems extinguish the flux at the expected wavelength of Lyα absorption, obtaining the largest targeted sample of DLA/sub-DLAs in low-redshift galaxies. We present absorption measurements of neutral hydrogen and metals. Additionally, we present Green Bank Telescope 21 cm emission measurements for five of the galaxies (including two detections). Combining our sample with the literature, we construct a sample of 117 galaxies associated with DLA/sub-DLAs spanning $0 < z < 4.4$, and examine trends between gas and stellar properties, and with redshift. The H I column density is anticorrelated with impact parameter and stellar mass. More massive galaxies appear to have gas-rich regions out to larger distances. The specific star formation rate (sSFR) of absorbing galaxies increases with redshift and decreases with M^*, consistent with evolution of the star formation main sequence (SFMS). However, $\sim$20% of absorbing galaxies lie below the SFMS, indicating that some DLA/sub-DLAs trace galaxies with longer-than-typical gas-depletion timescales. Most DLA/sub-DLA galaxies with 21 cm emission have higher H I masses than typical galaxies with comparable M^*. High M_{HI}/M^* ratios and high sSFRs in DLA/sub-DLA galaxies with $M^* < 10^9 M_\odot$ suggest these galaxies may be gas-rich because of recent gas accretion rather than inefficient star formation. Our study demonstrates the power of absorption and emission studies of DLA/sub-DLA galaxies for extending galactic evolution studies to previously under-explored regimes of low M^* and low SFR.

1. Introduction

An important challenge in current studies of galactic evolution is understanding how galaxies interact with the intergalactic medium (IGM) via inflows and outflows of gas. Inflows of relatively cool metal-poor gas can provide fresh fuel for star formation. At the same time, outflows driven by feedback from supernovae and active galactic nuclei (AGNs) can quench star formation. Both inflows onto galaxies and outflows from them pass through the circumgalactic medium (CGM). The CGM typically extends out to ~300 kpc around the galaxies, and serves as the interface between the galaxies and the IGM. Indeed, the CGM could contain a substantial fraction of the so-far elusive (so-called "missing") baryons from the galactic halos (e.g., Werk et al. 2014). Understanding how this CGM interacts with the galaxy's interstellar medium (ISM) is crucial in understanding the processes of star formation and feedback in galactic evolution.

Unfortunately, it is difficult to observe the gas in and around distant galaxies directly in its own light owing to its low density. An excellent solution to this problem is to study this gas in *absorption* rather than emission, in the spectra of bright background sources such as quasars. Especially important for such studies are the strongest of the absorption systems, i.e., the damped Lyα (DLA) and the sub-damped Lyα (sub-DLA) systems. The DLAs have neutral hydrogen column densities $N_{HI} \geqslant 2 \times 10^{20}$ cm^{-2}, while the sub-DLAs have $10^{19} \leqslant N_{HI} < 2 \times 10^{20}$ cm^{-2}. Over ~100,000 quasar absorption line systems, and $\gtrsim$12,000 candidate DLA/sub-DLAs have been discovered in the SDSS spectra of quasars (e.g., Noterdaeme et al. 2012b; York et al. 2022). DLAs and sub-DLAs provide the primary neutral gas reservoir for star formation (e.g., Péroux et al. 2005; Prochaska et al. 2005; Noterdaeme et al. 2009; Prochaska & Wolfe 2009; Noterdaeme et al. 2012b; Zafar et al. 2013; Popping et al. 2014). Furthermore, the DLAs and sub-DLAs offer the most reliable determinations of element abundances in distant galaxies (e.g., Pettini et al. 1997; Kulkarni et al. 2005; Pettini 2011; Rafelski et al. 2012; Som et al. 2015; Quiret et al. 2016).

Given the high H I content of DLAs and sub-DLAs, their relevance for galactic evolution studies is obvious. Indeed, DLAs and sub-DLAs are found to occur naturally in hydrodynamical simulations of structure formation, even out

---

[8] Enrico Fermi Institute, University of Chicago, Chicago, IL 60637, USA.

to a few hundred kiloparsecs from galaxy centers (e.g., Pontzen et al. 2008; Cen 2012; van de Voort et al. 2012; Rahmati & Schaye 2014; Nelson et al. 2020). Unfortunately, the connections between DLA/sub-DLAs and galaxies still remain far from clear, because even after decades of attempts to image the galaxies producing the absorbers (e.g., Kulkarni et al. 2001; Rao et al. 2003; Straka et al. 2010, 2011; Péroux et al. 2011; Krogager et al. 2017), only the galaxies associated with less than a few dozen DLA/sub-DLAs have been confirmed so far. As a result, a number of different scenarios exist for the origin of DLAs, ranging from galactic disks to gas-rich dwarf galaxies to subgalactic clumps (e.g., Wolfe et al. 1986; York et al. 1986; Jimenez et al. 1999; Zwaan et al. 2008; Fynbo et al. 2013; Zafar et al. 2014; Cooke et al. 2015).

The primary observational difficulty in detecting the galaxies associated with DLA/sub-DLAs in the continuum is that the absorbing galaxies are faint compared to the background quasars, and often at small angular separations from the quasars. This makes it difficult to reliably determine impact parameters, morphologies, sizes, structures, and star formation rates (SFRs) for the galaxies associated with the absorbers. These problems are especially challenging at high redshifts due to the $(1 + z)^{-4}$ dimming of surface brightness. A small sample of DLAs at $z > 2$ has been found to have host galaxies with disk-like properties (e.g., Djorgovski et al. 1996; Møller et al. 2002). On the other hand, based on kinematic similarities with the Local Group dwarf population, it has been suggested that the general $z \sim 3$ DLA population arises in metal-poor dwarf galaxies (Cooke et al. 2015). It has also been suggested that DLAs at $z \sim 3$ are similar to the outskirts of compact Lyman break galaxies with much lower star formation efficiencies than observed in local galaxies (e.g., Rafelski et al. 2011). Indeed, deep emission line imaging searches indicate that most high-z DLAs have low SFRs (e.g., Kulkarni et al. 2000, 2001, 2006; Christensen et al. 2009; Péroux et al. 2011).

The problems in detecting galaxies associated with DLA/sub-DLAs are easier to address at $z \lesssim 1$, where galaxy imaging is much easier. Indeed galaxies associated with some DLAs at $z < 1$ have been detected in broadband imaging studies (e.g., Bergeron & Boisse 1991; Le Brun et al. 1997; Rao et al. 2003) and in integral field spectroscopy (IFS; e.g., Péroux et al. 2011, 2014; Mackenzie et al. 2019; Péroux et al. 2019; Hamanowicz et al. 2020; Szakacs et al. 2021). Such studies suggest that even at $z < 1$, a substantial fraction of the galaxies associated with DLAs are dwarf galaxies. Indeed, $\sim 50\%$ of low-z DLAs appear to arise in galaxies with $L < 0.6L_*$; by contrast, observations of a few sub-DLAs at $z < 0.7$ show them all to be associated with $L > 0.6L_*$ disk-dominated galaxies (e.g., Zwaan et al. 2005). We note, however, that such comparisons are complicated by the detections of multiple galaxies in the fields of some absorbers (e.g., Kacprzak et al. 2010; Péroux et al. 2017, 2019; Hamanowicz et al. 2020).

Despite these successes, even at $z \sim 1$, galaxies associated with some DLAs remain undetected. Furthermore, even for galaxies that are detected, it can be difficult to determine the detailed stellar properties for comparison with the gas properties. The IFS studies often offer no measurement of the continuum. Samples of galaxies at redshifts $\lesssim 0.1$ can be probed at a much higher sensitivity that can uncover low surface brightness features, and are thus ideal for investigating the galaxy–CGM connection. An additional advantage is that at such low redshifts, the H I gas can also be detected directly

through its 21 cm line emission. Since the atomic gas component of galaxies extends much farther out than the stellar component and is more affected by environmental processes, these observations can provide additional inputs to understand the origins of the gas producing DLA/sub-DLAs (e.g., Carilli & van Gorkom 1992; Gupta et al. 2010; Dutta et al. 2017a). With this in mind, we have started targeting previously imaged galaxies at $z \lesssim 0.1$ with background quasars at small angular separations, and examining absorption lines at the redshifts of these galaxies in the quasar spectra. Recently, studies using the Sloan Digital Sky Survey (SDSS; York et al. 2000) have revealed such a sample of low-z galaxies on top of quasars (GOTOQs; Borthakur et al. 2010; Noterdaeme et al. 2010; York et al. 2012; Straka et al. 2013, 2015; Joshi et al. 2017).

GOTOQs are galaxies intervening with a background quasar for which part or all of the galaxy falls within the fibers of the SDSS spectrographs (with a diameter of $3''$ for the SDSS spectrograph and $2''$ for the Baryon Oscillation Spectroscopic Survey spectrograph). Star-forming galaxies in the redshift range $0 < z < 0.40$ can leave their imprints in optical quasar spectra in the form of nine strong, narrow galactic nebular emission lines ([O II] $\lambda 3727$, Hβ, [O III] $\lambda\lambda 4960,5008$, [N II] $\lambda 6550$, Hα, [N II] $\lambda 6585$, [S II] $\lambda\lambda 6718,6733$). Thus, GOTOQs are star-forming galaxies that are detectable in spectral absorption as well as emission, and are therefore well-suited for studying the environment of quasar absorption systems. For galaxies with $0.40 < z < 0.80$, optical spectra can cover the emission lines of [O II], Hβ, [O III], detection of which, together with Mg II absorption lines, can be used to confirm the galaxies. An automated search for these lines in over 100,000 SDSS quasar spectra led to a catalog of ~ 200 star-forming galaxies detected in these emission lines.

To investigate whether GOTOQs produce DLA/sub-DLAs, it is essential to obtain UV spectroscopy of the background quasars covering the Lyα absorption lines at the redshifts of the galaxies. Here we report results of Hubble Space Telescope (HST) Cosmic Origins Spectrograph (COS) observations of 10 star-forming galaxies at $z < 0.14$. The SDSS spectra of the 10 quasars show absorption features of Ca II H, K and/or Na I D1, D2 at the redshifts of some of these galaxies. Moreover, superposed on these quasar spectra are narrow nebular emission lines from the foreground galaxies that fall within the same SDSS spectral fiber as the quasar. The COS far-UV (FUV) spectra allow us to measure the Lyα absorption associated with these galaxies, providing a direct constraint on the incidence of DLA/sub-DLAs in galaxies of these morphologies and environments. Furthermore, the COS spectra allow us to make approximate assessments of the metal-line strengths, and to broadly search for any correlations between the gas properties inferred from the absorption features and the continuum and nebular emission properties of the galaxies. We also complement the SDSS and HST COS observations with H I 21 cm emission line observations of some of the galaxies to further understand the origin of absorbing gas with respect to these galaxies.

This paper is organized as follows: Section 2 details our sample selection and observations. Section 3 discusses the results of this study, including a summary of the characteristics of the individual objects in our sample in Section 3.1. Section 4 describes the results of our search for the H I 21 cm emission line using the Green Bank Telescope (GBT) in several of the

sample galaxies. Section 5 compares our results with those from the literature. Finally, Section 6 summarizes our conclusions. Throughout this paper, we adopt the concordance cosmology (Λ cold dark matter; $\Omega_m = 0.3$, $\Omega_\Lambda = 0.7$, and $H_0 = 70$ km s^{-1} Mpc^{-1}).

2. Observations and Data Reduction

2.1. Sample Selection

The SDSS images of each GOTOQ field in five optical broadband filters (ugriz) allow us to potentially resolve the morphology and geometry of these low-redshift galaxies. In 70% of cases in the parent sample (103 total), we detect a galaxy in the foreground of the quasar responsible for the nebular emission. [The remaining 30% of cases do not have imaging detections of galaxies and are likely extremely faint dwarf galaxies within the quasar point-spread function (PSF)].

Our HST COS targets consisted of 10 GOTOQs selected from this larger sample. To construct our HST sample, we first selected quasars from the parent sample that have GALEX FUV flux $>30\ \mu$Jy in order to provide an adequate S/N in a reasonable number of HST orbits, and have redshifts $z_{quasar} < 1.5$ to minimize the chances of intercepting an optically thick absorber along the line of sight, which would extinguish the flux below its Lyman limit at the wavelengths where Lyα from the GOTOQ would be expected. These criteria ruled out all but 13 of the quasars in our parent sample. Our only other selection criterion was that the galactic redshift be such that the Lyα line fell in a clean part of the COS grating, free of potential geocoronal emission lines. These criteria resulted in a subset of 10 GOTOQs suitable for COS observations of the H I Lyα absorption lines. The left panels of Figures 1 and 2 show the Dark Energy Camera Legacy Survey[9] (DECaLS; Dey et al. 2019) image thumbnails of our targets, centered on the background quasars. Figures 3 and 4 show the SDSS spectra of all of our target quasars, zoomed into the wavelength ranges containing the detected nebular emission lines produced by the foreground galaxies. Also shown are regions covering the Ca II H and K and Na I D absorption lines, although in most of these 10 sight lines, these absorption lines are elusive.

Our 10 GOTOQs have redshifts $z < 0.15$ and lie within impact parameters $\rho \lesssim 7$ kpc from the quasar lines of sight. They have active star formation with SFRs (estimated from Hα emission) in the range of 0.01–0.26 $M_\odot$ yr^{-1}. (We note that the SFRs could be higher than these estimates; we discuss the SFRs more in Section 2.2.2.) These galaxies range in luminosities from 0.02 L^* to 2.86 L^*, thus covering both dwarf and nondwarf galaxies, taking $L \lesssim 0.1L^*$ as the definition of a dwarf galaxy (Cimatti et al. 2020). Some of these galaxies also exhibit Ca II H, K or Na I D1, D2 absorption lines in the SDSS spectra of the background quasars. The SDSS data provide the emission line metallicities, dust reddening, and five-band optical photometry for each of these galaxies. As mentioned above, the quasar sight lines are at close enough impact parameters from the galaxy centers to potentially probe the inner regions of the galaxies, as can be seen in the left panels of Figures 1 and 2. Table 1 lists our targets and their characteristics. The galactic magnitudes are in the AB system (Oke & Gunn 1983) and have been corrected for foreground Milky Way extinction (Straka et al. 2015).

2.2. HST/COS Data

HST COS observations were obtained under program ID 14137 (PI: Straka). The FUV G140L grating was used with the central wavelength setting 1105 Å for seven quasar sight lines, and 1280 Å for the remaining three sight lines. Each quasar was observed for two orbits for total integration times ranging from 86 to 95 minutes. The foreground galaxies caused no problems with target acquisitions. All four focal plane positions (FP-POS) were used (two positions per orbit) to help mitigate fixed-pattern noise. For two of the 10 quasars observed, no flux was detected in the region of interest due to the presence of a previously unknown Lyman-limit system (LLS) at a higher redshift than that of the DLA of interest. For the remaining eight quasars, the COS spectra had adequate S/N. The G140L grating provides a spectral resolution of ~1500 (i.e., a velocity resolution of ~200 km s^{-1}) at ~1350 Å. This resolution is adequate for detecting broad absorption lines, such as the Lyα lines in the DLAs/sub-DLAs hosted by the GOTOQs, and also enables approximate measurements of metal absorption lines (even if unresolved) arising in these galaxies.

2.2.1. HST COS Spectral Analysis

Each HST COS exposure was reduced and extracted with the Space Telescope Science Data Analysis System COS pipeline. The individual extracted one-dimensional spectra were coadded. The quasar continuum was fitted, and absorption line measurements were performed on the continuum-normalized spectra. In order to derive an H I column density and absorption velocity from the Lyα line, we first normalized the continuum of the quasar flux by fitting Legendre polynomials to wavelength ranges free from emission or absorption features (e.g., Sembach & Savage 1992). While establishing a best-fit continuum to the data, this method also generates $\pm 1\sigma$ different fits, which we refer to as "upper" and "lower" error envelopes, which can also be used to normalize the data. We constructed theoretical Lyα Voigt profiles with initial estimates of the H I column densities N_{HI}, velocity offsets Δv relative to the galactic redshifts (the latter defined by the nebular emission lines), and Doppler parameters, and varied these to fit the Lyα absorption in the spectrum normalized by the best-fit continuum, as well as by the upper and lower envelopes (Bowen et al. 2008; Bowen et al. 2016). Theoretical COS G140L line spread functions were convolved with the Voigt line profiles, but in most cases, the Lyα absorption observed was so broad and the H I column density so high that both the LSF widths and the Doppler parameters were too small to make an appreciable difference to the final estimates of the column densities.

Values of N_{HI} and Δv are given in Table 3. Errors in N_{HI} come from the difference between the values of N_{HI} derived from the upper and lower envelope fits to the continuum, and the best fit, and are significantly larger than any errors arising from Poisson statistics in the data alone. The right panels in Figures 1 and 2 show the best-fitting Voigt profiles and $\pm 1\sigma$ profiles obtained for each of the absorbers. Seven of the eight absorbers are found to be DLAs, and one is found to be a sub-DLA.

Table 2 lists the metal-line measurements detected at $\gtrsim 3\sigma$ level performed using the program SPECP[10] on the COS
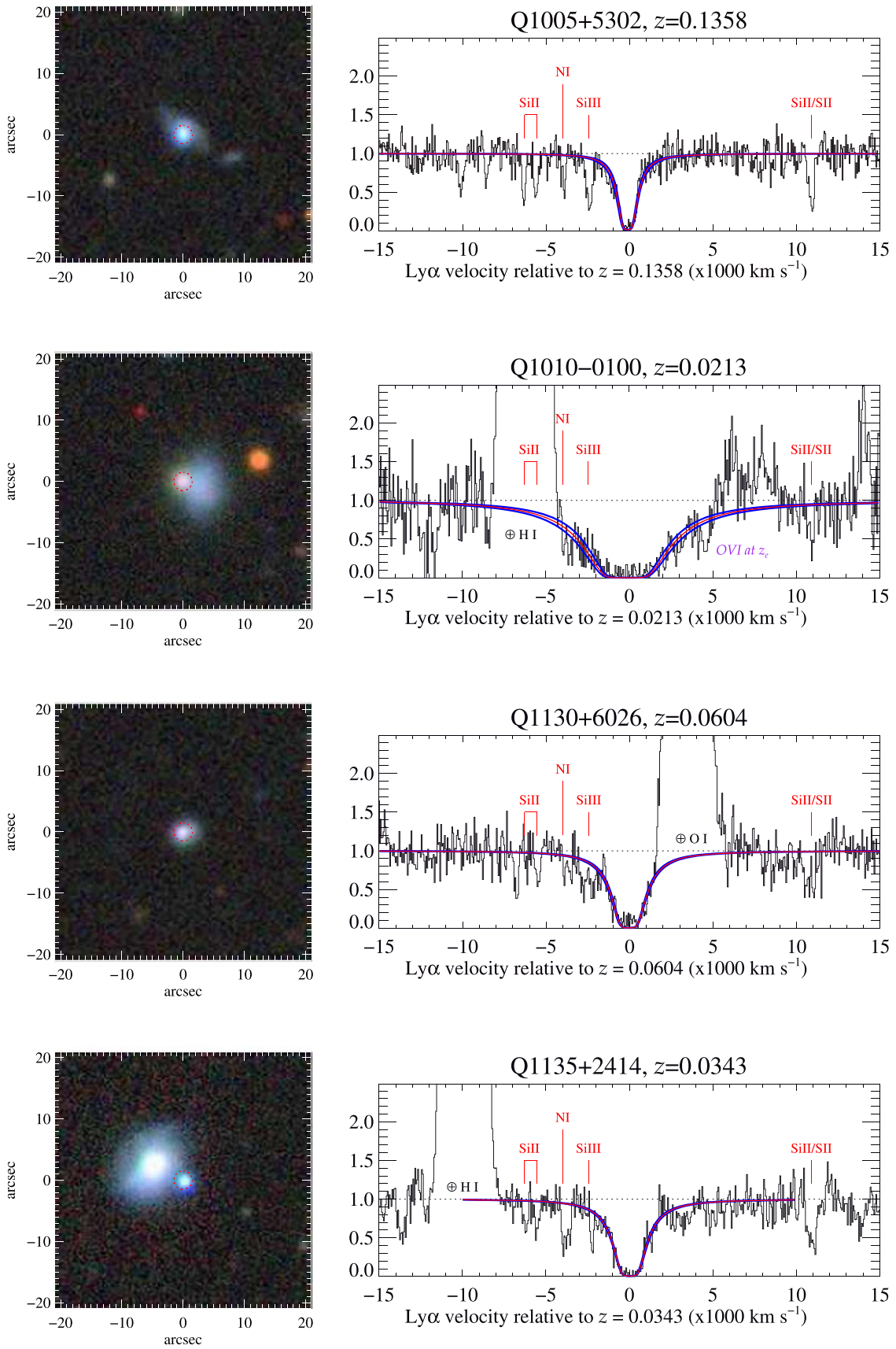
Figure 1. Four of the quasar–galaxy pairs in our sample. The images show *grz*-band cutouts of each of the quasar–galaxy pairs, taken from DR9 of the Dark Energy Camera Legacy Survey (DECaLS; Dey et al. 2019). Each image is centered on the coordinates of the quasar, and a red dotted circle indicates the area of the 3″ diameter fibers used by SDSS to observe the quasar and galaxy. Also shown are portions of the G140L spectra of the quasars showing the strong Lyα absorption detected in the rest frame of the foreground galaxy. Voigt profile fits to the Lyα lines are shown as red lines, and the associated errors in the fits as purple lines. Geocoronal emission features and broad emission lines from the quasars are indicated. Metal absorption lines of Si II, Si III, N I, and S II from the foreground galaxy, which are close to the wavelength of Lyα, are also indicated, but full details of the metal-line absorption are given in Table 2.

spectra for the eight absorbers for which the H I Lyα is covered. While the spectral resolution of our COS spectra is not adequate to obtain reliable metal column densities, the equivalent widths of the metal lines are well determined and are expected to be reliable. The quasar continuum was first fitted globally with a cubic spline polynomial (typically of the order of one to two) using the IRAF task CONTINUUM. The continuum placement was refined locally near each line in SPECP before measuring the equivalent widths. For each measured feature, Table 2 also lists the 1σ uncertainty in the equivalent width due to photon noise, the 1σ uncertainty due to the continuum measurement uncertainty, the combined 1σ uncertainty (obtained by adding in quadrature the photon noise and continuum measurement uncertainties), and the significance of the feature.

2.2.2. SDSS Measurements

The SDSS fiber of $3''$ diameter allows us to estimate emission line properties of the galaxy in approximately the same area as the COS circular aperture ($2''5$ in diameter). Below we review the spectral and photometric measurements made for these galaxies from SDSS data, but refer the reader to our past papers (York et al. 2012; Straka et al. 2013, 2015) for more detailed discussion on the topic.

Detections of [O II] and Hα emission lines allow us to estimate the SFR following the standard prescriptions (Kennicutt 1998):

$$SFR_{[O\,II]}\ (M_\odot\ \mathrm{yr}^{-1}) = 1.4 \times 10^{-41}\ L_{[O\,II]}\ (\mathrm{ergs\ s}^{-1}) \quad (1)$$

$$SFR_{H\alpha}\ (M_\odot\ \mathrm{yr}^{-1}) = 7.9 \times 10^{-42}\ L_{H\alpha}\ (\mathrm{ergs\ s}^{-1}), \quad (2)$$

where $L_{[O\,II]}$ and $L_{H\alpha}$ are the luminosities in [O II] $\lambda3727$ and Hα emission. We use the five-band imaging from SDSS to estimate the photometric reddening, $E(B-V)_{(g-i)}$, for each galaxy as a whole. Using the Balmer decrement, we are also able to estimate the line-of-sight reddening, $E(B-V)_{H\alpha/H\beta}$. We correct for this reddening and also for the Milky Way extinction in each sight line. Table 1 lists the resultant SDSS SFR measurements.

We note that the total SFR in the galaxy may be different from the above estimates, partly because the continuum of the galaxy is not known, since these lines are found superimposed on the quasar spectrum itself. However, the continuum contribution error is generally likely to be relatively low. The more significant reason the SFRs derived from the SDSS spectra may not be accurate is that the SDSS fiber itself typically probes only a fraction of the galaxy's projected surface area, except in the case of the very smallest galaxies. The low resolution of the SDSS images makes it difficult to precisely quantify what fraction of the galactic surface area is covered by the SDSS fiber. We have, nevertheless made rough estimates of the SFR for the whole galaxy by scaling the dust-corrected SFRs estimated from the SDSS spectra by the ratio of the galaxy's projected area as determined from the DECaLS images, and the projected area of the fiber, since in each of our fields, the angular separation of the quasar from the galaxy center is less than or nearly equal to the projected semimajor axis of the galaxy in arcseconds. The corrections thus estimated are substantial (more than a factor of 10) for four of our galaxies. These corrections are not precise, both because the DECaLS images are also modest in their spatial resolution, and because the SFR is unlikely to be uniform across the entire

galaxy; however, the SFRs including these crude corrections are an improvement over the SFRs estimated purely from the SDSS spectra. In all of the statistical analysis presented in Section 5, we use these "fiber loss-corrected" SFRs.

The distribution of stellar masses, estimated from the SDSS photometric data by Straka et al. (2015) from fitting stellar population synthesis models (see Section 5.4.1 for more details) has a wide range ($7.31 \leqslant \log M^*/M_\odot \leqslant 9.78$) with a mean stellar mass of $\log M^*/M_\odot = 9.40 \pm 0.36$. However, we caution that these stellar mass estimates can be quite uncertain given the limited photometric information we have for these targets. Currently no near-infrared or UV photometric data are available, and the SDSS images are quite shallow. Also, although we have performed PSF subtraction in all cases to remove the quasar contribution to the flux, the spatial resolution and depth of the SDSS images are not sufficient to obtain robust spectral energy distributions (SEDs) for our galaxies.

3. Results

3.1. Individual Objects

3.1.1. Q0902+1414

The COS spectrum for this quasar shows little, if any, flux. However, around 1500–1700 Å, there is a gradual drop-off in the low-level flux present, indicating there is likely a partial Lyman-limit system (LLS) around $z_{LLS} \sim 0.6$ cutting off the flux below its Lyman limit. The GALEX FUV flux for this quasar is among the lowest in our sample (38 μJy), and the redshift path length between the quasar and the galaxy is among the largest ($\Delta z = 0.9295$), supporting the hypothesis that a higher-z LLS is blocking the quasar flux. Indeed, the SDSS spectrum of Q0902+1414 shows a potential system at $z = 0.633$ with Mg I, Mg II, and Fe II absorption. We do no further analysis on the COS spectrum of this sight line. The DECaLS image of this galaxy shows an edge-on geometry with the quasar probing the north edge of the galactic disk (Figure 2).

3.1.2. Q1005+5302

We detect broad hydrogen absorption and metal lines associated with the foreground galaxy. Our H I column density measurements show a sub-DLA in this sight line with $\log N_{HI} = 20.08^{+0.08}_{-0.07}$. Absorption features near the expected positions of the transitions for a number of low and intermediate metal ions (e.g., C I, C II, N I, O I, Al II, Si II, Si III, S II, Ni II, and Co II) and high ions (C IV and Si IV) are also detected.

In an earlier work (Straka et al. 2015), we detected excess flux from the galaxy after quasar PSF subtraction, but were not able to determine the morphology or geometry of this galaxy due to its extremely small size and overlapping proximity to the quasar. Thus, the quasar appears to be directly probing the main body of the galaxy. See Figure 1.

3.1.3. Q1010-0100

The color of this quasar is extremely red, suggesting the presence of a large quantity of dust. The DLA along this sight line is flanked by geocoronal Lyα emission on the blue side and quasar O VI emission on the red side. We have left the quasar O VI emission in for the continuum fit of the spectrum. This is the strongest DLA in our sample with $\log N_{HI} = 21.38 \pm 0.07$. Absorption features near the expected positions of the transitions for several metal ions (e.g., C I, C II, O I, Mg I, Si II, and Ni II) are
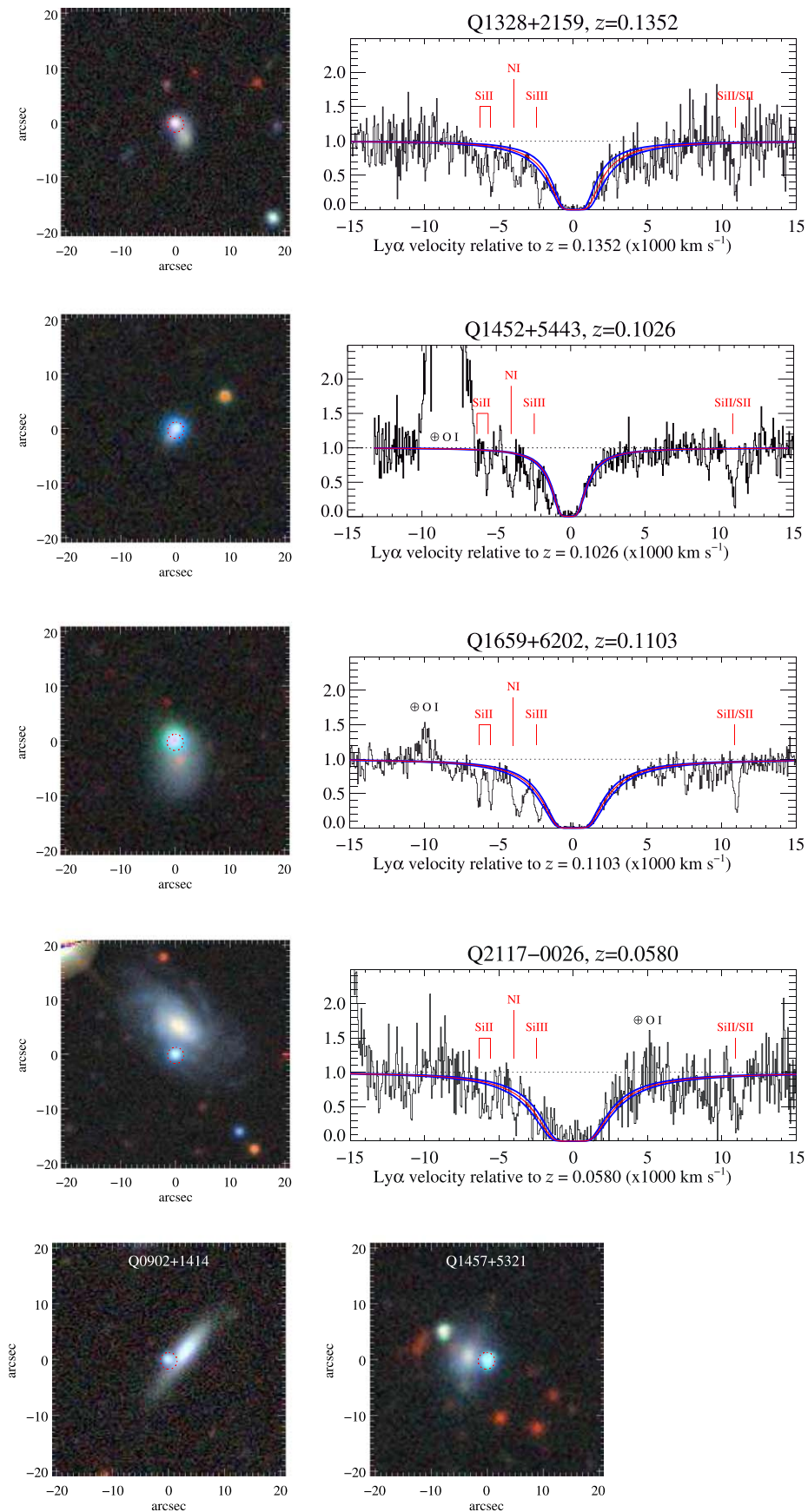
Figure 2. Same as Figure 1, for our remaining quasar–galaxy pairs. No G140L spectra are shown for the two targets for which no detectable flux exists near the Lyα absorption owing to a higher-redshift Lyman-limit system.
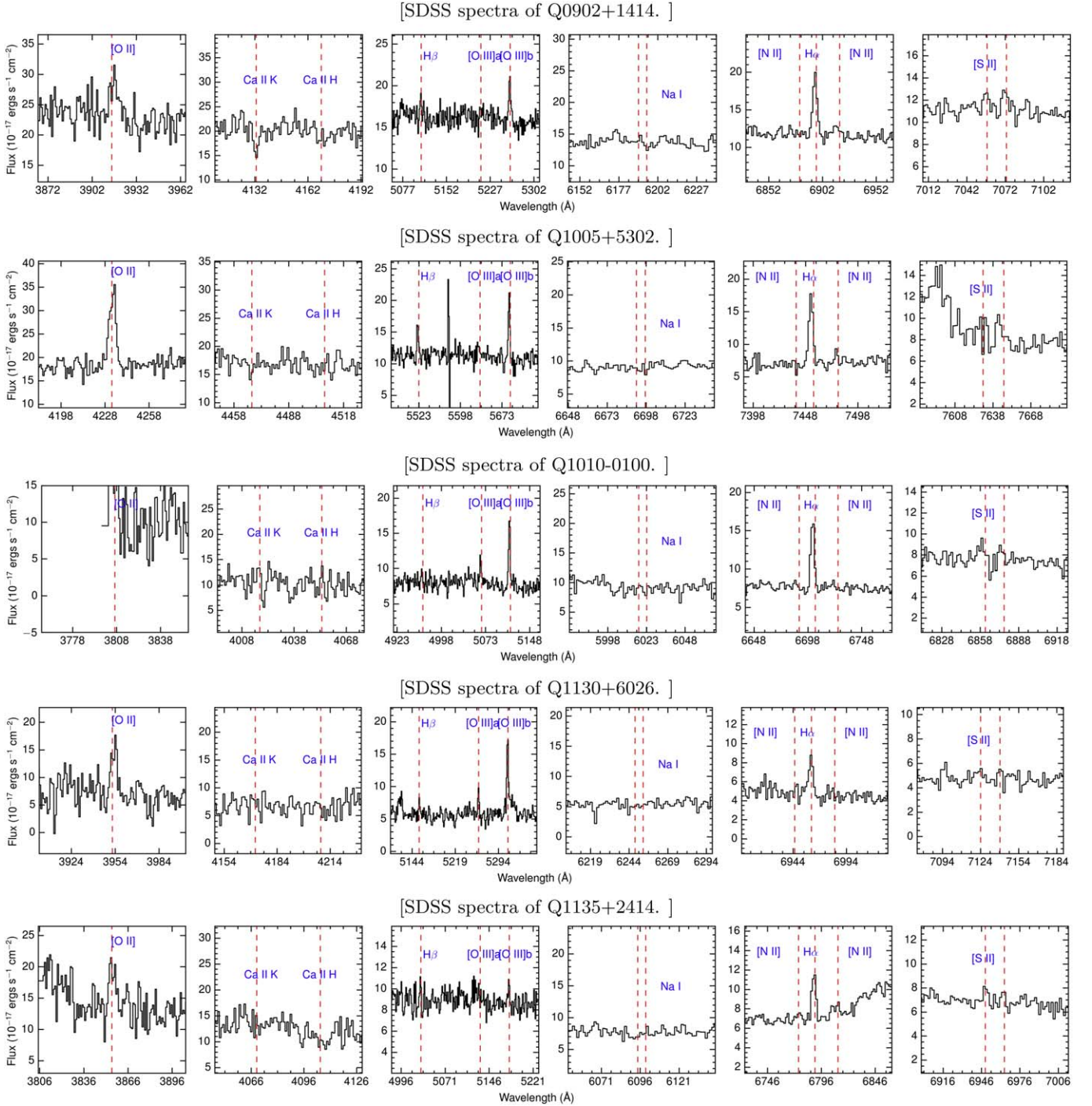
Figure 3. SDSS spectra of five of our target quasars. Dashed red lines mark the expected wavelengths of the nebular emission lines and the Ca II, Na I absorption lines from the foreground galaxies.

also detected. Figure 1 suggests a face-on galactic geometry with the quasar probing the outskirts of the visible disk.

3.1.4. Q1130+6026

We detect a DLA at the redshift of the foreground galaxy. There is contamination in the red wing of the DLA from geocoronal O I emission, as the absorption lies right against the emission line. This strongly affects the continuum fit for this system, and thus potentially causes an underestimation in the H I column density and errors in the fit compared to our other sight lines. With this in mind, we report a column density of log

$N_{HI} = 20.57 \pm 0.04$. Absorption features near the expected positions of the transitions for a number of low and intermediate metal ions (e.g., C II, N I, N V, O I, Al II, Si II, Ni II, and Co II) are also detected. As seen in Figure 1, the foreground galaxy is too small to reliably determine morphology or geometry in this case.

3.1.5. Q1135+2414

The COS spectrum shows a DLA with log $N_{HI} = 20.57 \pm 0.03$. Absorption features near the expected positions of the transitions for a number of low and intermediate metal ions (e.g., C I, C II, C IV, N I, O I, Al II, Si II, Si III, Si IV, S II,
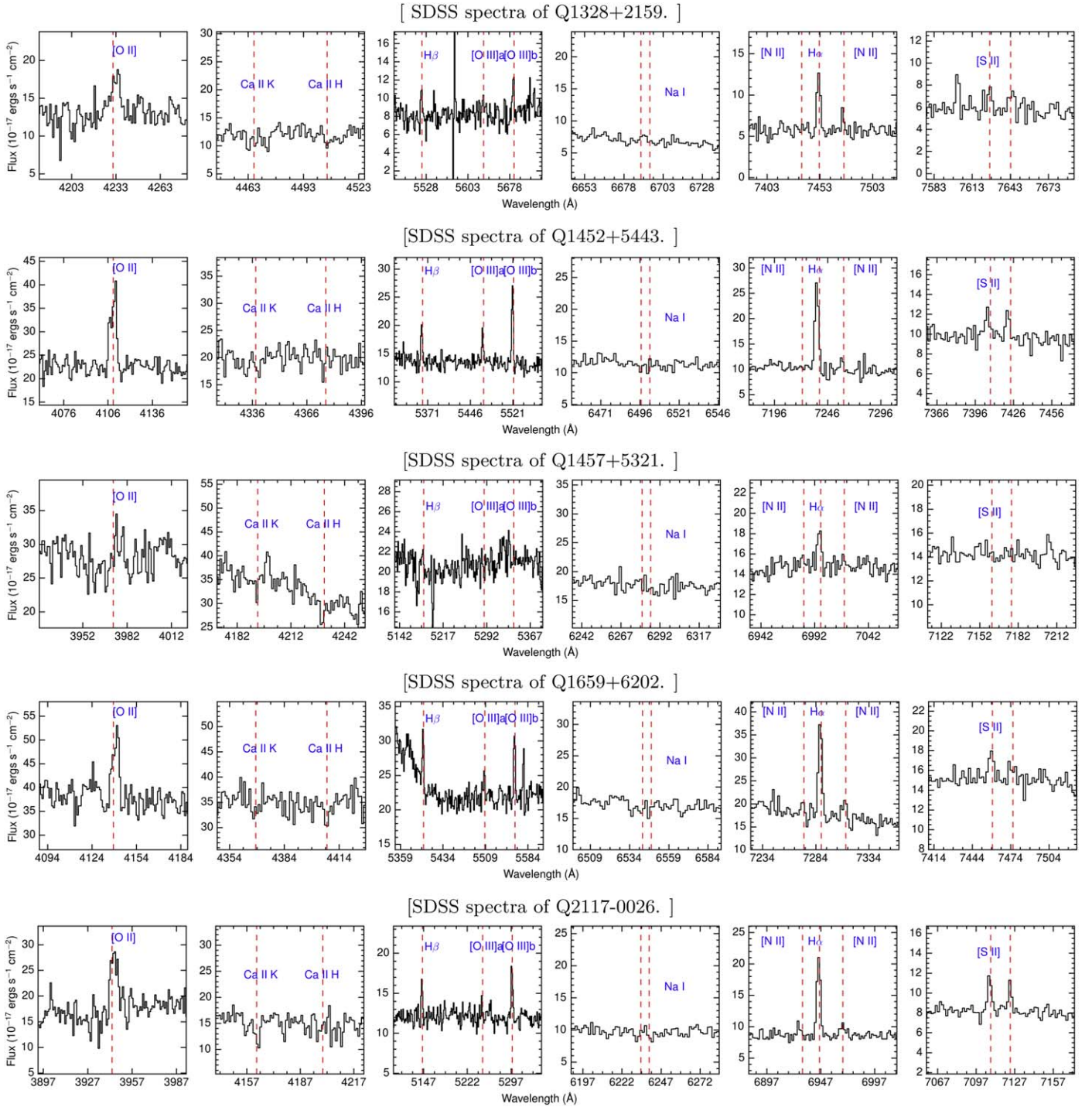
Figure 4. Same as Figure 3, for our remaining target quasars.

Ni II, and Fe II) are also detected. As seen in Figure 1, this quasar probes a region ~4 kpc from the center of a mostly face-on galaxy, on the outskirts of the star-forming disk. According to the photometric properties derived from the SDSS *r*-band image, this galaxy is highly luminous with $L/L^* = 2.86$.

3.1.6. Q1328+2159

For this target, the redshift of the galaxy was suitable to cover the wavelength ranges of both Lyα and Lyβ absorption. The spectrum shows a DLA in the blue wings of the background quasar's O VI emission line. We estimate $\log N_{HI} = 21.01 \pm 0.11$ from the Lyα and Lyβ absorption lines. Absorption features near the expected positions of the transitions for a number of low or intermediate metal ions (e.g., C I, C II, N I, O I, Al II, Si II, Si III, S II, Ni II, and Fe II) as well as high ions (C IV, N V, and Si IV) are also detected. Additionally, this system shows possible O VI absorption at the redshift of the galaxy. The small size of this galaxy seen in Figure 2 prevents us from reliably determining the geometry or morphology.

Table 1
Quasar–Galaxy Pairs Observed with HST COS

Quasar	R.A., Decl. (J2000)	z_{quasar}	z_{gal}	f $^1_{Ly\alpha}$ (cgs)	$m_{r\ gal}$	L/L^*2_r	log M^{*3} ($M_\odot$)	θ^4 ($''$)	ρ^5 (kpc)	SFR$^6_{SDSS}$ ($M_\odot$ yr^{-1})	Ref, ID^7
Q0902+1414	09:02:50.47, 14:14:08.29	0.980	0.0505	<0.1	17.41	1.21	9.65	3.6	3.6	0.03	S15, 4
Q1005+5302	10:05:14.21, 53:02:40.04	0.560	0.1358	7.0	19.50	0.31	9.60	1.5	3.6	0.19	Y12, 12
Q1010-0100	10:10:15.74, −01:00:38.11	0.230	0.0213	1.5	17.91	0.03	8.88	2.9	1.2	0.04	Y12, 2
Q1130+6026	11:30:02.99, 60:26:28.62	0.370	0.0604	4.0	20.28	0.02	7.31	1.7	2.0	0.02	S13, 15
Q1135+2414	11:35:55.66, 24:14:38.10	1.450	0.0343	4.0	16.48	2.86	9.41	5.7	3.9	0.01	S15, 18
Q1328+2159	13:28:24.33, 21:59:19.66	0.330	0.1352	2.5	19.12	0.25	9.06	2.4	5.7	0.16	S15, 31
Q1452+5443	14:52:40.53, 54:43:45.11	1.520	0.1026	4.0	⋯	⋯	7.96	1.9	3.6	0.25	Y12, 18
Q1457+5321	14:57:19.00, 53:21:59.27	1.200	0.0660	<0.1	17.95	0.74	9.28	3.4	4.2	0.04	S15, 40
Q1659+6202	16:59:58.94, 62:02:18.14	0.230	0.1103	13	18.53	0.48	9.78	3.6	7.2	0.26	S13, 24
Q2117-0026	21:17:01.31, −00:26:38.80	1.137	0.0580	1.9	17.32	0.38	9.64	5.1	5.7	0.04	S13, 25

Note. 1. Continuum flux of the background quasar in units of 10^{-16} erg s^{-1} cm^{-2} Å^{-1} near the wavelength of the Lyα absorption from the foreground galaxy, as measured in our HST COS spectra. 2. The r-band L/L^* values of our foreground galaxies found in SDSS. Values <0.2 are considered dwarf galaxies. No value is listed for Q1452+5443 since the SDSS images do not resolve the foreground galaxy. 3. Stellar mass of the galaxy, adopted from Straka et al. (2015). 4. Angular separation of the galaxy from the sight line of the quasar in arcseconds, determined from the SDSS images, except for Q1452+5443 where the value measured from DECaLS images is listed. 5. Impact parameter of the galaxy with the sight line of the quasar in kiloparsecs determined from the SDSS images, except for Q1452+5443 where the value measured from DECaLS images is listed. 6. Dust-corrected SFR determined from Hα emission line flux detected in the SDSS fibers, from Straka et al. (2015). 7. Reference for galactic magnitude and the ID number for the galaxy in that reference. Y12: York et al. (2012), S13: Straka et al. (2013); S15: Straka et al. (2015).

3.1.7. Q1452+5443

The redshift of this foreground galaxy allows for the use of Segment B. We detect a DLA with log $N_{HI} = 20.66^{+0.04}_{-0.03}$ cm^{-2}, constrained by the detection of Lyβ. No O VI absorption is detected in Segment B, though we detect absorption features near the expected metal-line positions for a number of low ions (e.g., C I, C II, N I, O I, Al II, Si II, Si III, S II, Ni II, Fe II, and Co II) as well as high ions (C IV and Si IV). Additionally, there is an absorption line at $\lambda1334$ Å that may be additional Lyα at more negative velocities, another interloping absorption system at a different redshift, or simply C II λ 1334 in the Milky Way interstellar medium. We exclude this absorption feature from our H I column density estimation.

This system is unique among our sample GOTOQs, as it has no detectable galaxy (in continuum light) in the SDSS images in any of the five filters. The upper limit on the stellar mass from photometric noise estimates outside the quasar PSF is log($M^*/M_\odot$) < 8.0. From the SDSS images, this quasar–galaxy configuration seems to be similar to two other pairs in this sample, Q1005+5302 and Q1130+6026. Both of the latter sight lines have compact galaxies that are difficult if not impossible to distinguish without proper quasar PSF subtraction. However, in the case of Q1452+5443, Straka et al. (2015) were unable to detect the foreground galaxy in the SDSS images even after PSF subtraction.

We therefore examined the DECaLS images of this field (deeper than the SDSS images), and found them to show a faint galaxy slightly offset from the quasar. We performed PSF subtraction on the r-band DECaLS image using a star in the same image for the PSF. The PSF-subtracted image shows an offset of $1\rlap{.}''9$ between the quasar and the brightest visible part of the galaxy, implying an impact parameter of 3.6 kpc at the redshift of the GOTOQ.

3.1.8. Q1457+5321

We detect no continuum flux from this quasar in the HST COS spectrum near the expected position of the Lyα

absorption in the foreground galaxy at $z_{gal} = 0.0660$, and in fact a very low flux level below ~1800 Å. The GALEX FUV flux for this quasar is among the lowest in our sample, (39 μJy), and the redshift difference between the quasar and the galaxy is among the largest ($\delta z = 1.134$). The combination of these two factors likely indicates the presence of an LLS at $z \sim 1$. Indeed, the SDSS spectrum of Q1457+5321 shows a potential system at $z = 0.99$ with Mg I, Mg II, and Fe II absorption. We do no further analysis on the COS spectrum of this sight line.

3.1.9. Q1659+6202

This galaxy appears to be roughly face-on, and has the highest stellar mass among our GOTOQs. We detect a DLA in this sight line with log $N_{HI} = 21.20^{+0.07}_{-0.05}$. Absorption features near the expected positions of metal lines for many low ions (e.g., C I, C II, N I, O I, Si II, P II, S II, and Ni II) as well as Si IV are detected for this system.

3.1.10. Q2117+0026

We detect a DLA in this sight line with log $N_{HI} = 21.35^{+0.07}_{-0.06}$. There is some contamination from geocoronal O I emission in the red wing of the DLA. Absorption features near the expected positions of the metal lines for several low ions (e.g., C II, N I, O I, Si II, and S II) as well as high ions (C IV, N V, and Si IV) are detected for this system.

3.2. Lyα Emission

The SDSS fiber aperture and the COS aperture probe roughly the same region of the galaxy, being $3''$ and $2\rlap{.}''5$ in diameter, respectively. Since we find strong nebular emission lines associated with the galaxy in this small region indicating active star formation, we might expect to find Lyα emission also. Indeed, previous works at $2 < z < 4$ have found Lyα emission in the troughs of individual DLAs (e.g., Noterdaeme et al. 2012a; Kulkarni et al. 2012, 2015) and in stacked spectra of DLAs with log $N_{HI} > 21.0$ (e.g., Noterdaeme et al. 2014;

Table 2
Metal-line Measurements for the DLA/Sub-DLAs in the COS Spectra

Quasar	λ_{obs} (Å)	W_{obs}^1 (mÅ)	$\sigma W_{obs}^{phot,2}$ (mÅ)	$\sigma W_{obs}^{cont,3}$ (mÅ)	$\sigma W_{obs}^{tot,4}$ (mÅ)	$W^5/\sigma W_{tot}$	Ion	λ_{rest}
Q1005+5302	1108.892	1788.65	292.86	171.44	339.35	5.3	O I	976.448
	1123.251	1523.63	186.05	170.24	252.19	6.0	O I	988.773
	1176.995	2867.97	265.16	261.89	372.68	7.7	C II	1036.336
	1287.801	289.07	53.00	43.95	68.85	4.2	N I	1134.980
	1351.561	740.60	37.90	35.39	51.85	14.3	Si II	1190.415
	1354.938	734.41	40.11	42.39	58.36	12.6	Si II	1193.289
	1362.602	468.06	37.89	43.30	57.54	8.1	N I	1199.549
	1369.652	1159.75	44.84	45.97	64.22	18.1	Si III	1206.500
	1420.093	392.88	32.38	37.67	49.68	7.9	S II	1250.578
	1423.493	264.16	28.81	31.02	42.33	6.2	S II	1253.805
	1429.803	255.39b	24.73	21.31	32.65	7.8	S II	1259.518
	1431.017	1028.38b	31.01	17.62	35.66	28.8	Si II	1260.422
	1478.377	711.24	52.72	56.65	77.39	9.2	O I	1302.168
	1480.637	732.69	58.95	76.79	96.80	7.6	Si II	1304.370
	1495.201	177.41	31.51	23.16	39.10	4.5	Ni II	1317.217
	1508.578	187.61	38.59	37.74	53.98	3.5	C I	1328.833
	1514.666	1629.26b	61.42	51.52	80.16	20.3	C II	1334.532
	1516.344	352.85b	42.27	40.41	58.48	6.0	C II*	1335.707
	1581.801	644.88	56.75	50.09	75.69	8.5	Si IV	1393.760
	1592.546	226.20	48.40	47.70	67.96	3.3	Si IV	1402.772
	1645.636	415.14b?	73.48	72.76	103.41	4.0	Co II	1448.019
	1650.646	295.69	65.73	60.52	89.35	3.3	Ni II	1454.842
	1667.570	275.18	67.75	66.75	95.11	2.9	Ni II	1467.756
	1680.841	309.37	61.46	43.05	75.04	4.1	Co II	1480.954
	1733.266	666.14	88.71	88.23	125.12	5.3	Si II	1526.707
	1757.432	603.73	83.41	61.07	103.37	5.8	C IV	1548.204
	1760.094	127.16	62.17	49.69	79.59	1.6	C IV	1550.781
	1771.365	341.38	76.14	63.13	98.91	3.5	C I	1560.309
	1881.290	269.29	76.65	61.40	98.21	2.7	C I	1656.928
	1896.862	461.32	85.03	64.92	106.98	4.3	Al II	1670.788
Q1010-0100	1286.944	544.46	96.07	89.10	131.03	4.2	Si II	1260.422
	1329.792	597.68	112.32	71.56	133.18	4.5	O I	1302.168
	1333.477	362.52	105.07	80.01	132.06	2.7	Si II	1304.370
	1362.575	617.21	114.44	77.05	137.96	4.5	C II	1334.532
	1367.030	461.28b?	100.06	60.07	116.71	4.0	C II*	1335.707
	1593.518	1539.74	230.43	210.75	312.27	4.9	C I	1560.309
	1777.170	1407.64	326.32	227.88	398.01	3.5	Ni II	1741.553
	1785.543	501.86	178.75	48.95	185.33	2.7	Mg I	1747.793
Q1130+6026	1262.454	209.25	41.04	33.26	52.83	4.0	Si II	1190.415
	1265.428	570.90	63.80	77.42	100.32	5.7	Si II	1193.289
	1272.433	275.15	50.26	51.64	72.06	3.8	N I	1199.549
	1273.901	259.41b?	45.89	41.67	61.99	4.2	N I	1200.223
	1314.466	408.24	65.87	73.58	98.76	4.1	N V	1238.821
	1317.113	136.34	45.56	38.29	59.51	2.3	N V	1242.804
	1336.447	429.06	54.94	43.57	70.12	6.1	Si II	1260.422
	1380.934	517.94	55.67	52.64	76.61	6.8	O I	1302.168
	1383.399	735.70	63.12	64.44	90.20	8.2	Si II	1304.370
	1415.262	303.29	54.33	58.96	80.17	3.8	C II	1334.532
	1553.652	402.93	82.57	67.77	106.82	3.8	Co II	1466.211
	1555.467	394.59	79.95	62.20	101.29	3.9	Ni II	1467.259
	1570.084	379.03	65.27	32.27	72.82	5.2	Co II	1480.954
	1653.712	448.95	107.33	125.06	164.81	2.7	C I	1560.309
	1756.726	584.00	130.23	69.86	147.79	4.0	C I	1656.928
	1813.409	726.43	134.82	61.14	148.03	4.9	Ni II	1709.604
	1890.756	961.66	261.48	128.27	291.25	3.3	P I	1782.829
	1896.507	683.70	189.70	24.39	191.26	3.6	P I	1787.648
Q1135+2414	1173.254	837.39	85.85	109.14	138.85	6.0	N I	1134.980
	1184.169	425.50	75.71	97.25	123.24	3.5	Fe II	1144.937
	1195.672	257.11	62.36	67.72	92.06	2.8	C I	1155.809
	1231.278	494.57	53.35	61.97	81.77	6.0	Si II	1190.415
	1234.175	498.62	52.32	58.66	78.66	6.3	Si II	1193.289
	1240.691	497.20	40.52	27.28	48.85	10.2	N I	1199.549
	1241.627	401.57b	36.25	21.67	42.23	9.5	N I	1200.223

Table 2
(Continued)

Quasar	$\lambda_{\rm obs}$ (Å)	$W_{\rm obs}^1$ (mÅ)	$\sigma W_{\rm obs}^{\rm phot,2}$ (mÅ)	$\sigma W_{\rm obs}^{\rm cont,3}$ (mÅ)	$\sigma W_{\rm obs}^{\rm tot,4}$ (mÅ)	$W^5/\sigma W_{\rm tot}$	Ion	$\lambda_{\rm rest}$
	1242.362	355.06	36.25	23.53	43.22	8.2	N I	1200.709
	1248.032	589.87	46.79	39.29	61.10	9.7	Si III	1206.500
	1293.760	261.32b?	48.26	55.93	73.87	3.5	S II	1250.578
	1296.946	942.40b?	68.25	94.98	116.96	8.1	S II	1253.805
	1303.423	468.56b	58.64	79.24	98.58	4.8	Si II	1260.422
	1347.071	591.12	48.71	36.17	60.67	9.7	O I	1302.168
	1348.950	794.46	60.75	61.75	86.62	9.2	Si II	1304.370b
	1380.658	681.96	59.91	53.81	80.53	8.5	C II	1334.532
	1441.647	335.00	53.02	38.67	65.63	5.1	Si IV	1393.760
	1449.950	280.40b?	56.96	50.60	76.19	3.7	Si IV	1402.772
	1462.950	179.48	53.02	47.43	71.14	2.5	Ga II	1414.402
	1579.564	1738.11	156.91	187.03	244.14	7.1	Si II	1526.707
	1591.126	1228.62b?	129.40	123.20	178.67	6.9	Si II*	1533.431
	1601.577	691.27	104.08	88.56	136.66	5.1	C IV	1548.204
	1603.635	389.36	91.49	80.79	122.05	3.2	C IV	1550.781
	1612.704	342.32	76.91	46.60	89.93	3.8	C I	1560.309
	1663.800	633.27	95.61	62.72	114.35	5.5	Fe II	1608.451
	1714.113	142.93	61.34	36.33	71.29	2.0	C I	1656.928
	1728.560	800.06	108.76	82.90	136.76	5.9	Al II	1670.788
	1737.626	654.82	101.08	74.83	125.76	5.2	P I	1679.696
	1761.507	369.94	99.14	57.19	114.45	3.2	Ni II	1703.411
Q1328+2159	1123.523	2031.42b	588.96	406.42	715.57	2.8	Si II	989.873
	1171.543	763.93	223.87	77.64	236.96	3.2	O VI	1031.926
	1177.093	2983.72	438.33	290.52	525.86	5.7	C II	1036.336
	1287.867	751.99	116.43	117.85	165.66	4.5	N I	1134.414
	1299.963	261.83	65.31	80.54	103.69	2.5	Fe II	1144.937
	1308.604	81.56	13.56	10.01	16.85	4.8	P II	1152.818
	1312.193	398.92	73.99	93.87	119.52	3.3	C I	1155.809
	1351.215	774.32	91.98	137.17	165.15	4.7	Si II	1190.415
	1354.667	793.15	75.11	76.36	107.10	7.4	Si II	1193.289
	1362.543	1143.60	66.37	84.34	107.32	10.7	N I	1199.549
	1369.706	1049.62	57.51	56.84	80.86	13.0	Si III	1206.500
	1407.496	425.55	91.66	117.80	149.26	2.9	N V	1238.821
	1410.345	337.65	69.29	61.02	92.33	3.7	N V	1242.804
	1423.638	196.75	56.11	43.27	70.86	2.8	S II	1253.805
	1430.594	1363.88	105.66	110.07	152.58	8.9	Si II	1260.422
	1478.275	596.06	96.05	96.98	136.49	4.4	O I	1302.168
	1481.245	474.28b	78.43	58.85	98.06	4.8	Si II	1304.370
	1515.329	1572.56	160.66	185.82	245.64	6.4	C II	1334.532
	1582.422	1072.72b?	93.86	129.06	159.58	6.7	Si IV	1393.760
	1603.268	148.44	34.83	30.53	46.32	3.2	Ni II	1412.866
	1605.737	105.30	28.43	20.10	34.82	3.0	Ga II	1414.402
	1757.356	1363.27	158.70	73.00	174.69	7.8	C IV	1548.204
	1759.953	1018.83	161.85	125.54	204.83	5.0	C IV	1550.781
	1825.907	1047.00	158.57	52.65	167.08	6.3	Fe II	1608.451
	1896.112	1640.99	291.16	163.73	334.04	4.9	Al II	1670.788
Q1452+5443	1171.726	690.91b?	189.44	128.35	228.83	3.0	Fe II	1063.176
	1312.090	247.47	40.60	35.38	53.86	4.6	Si II	1190.415
	1315.236	577.85b?	49.70	44.42	66.66	8.7	Si II	1193.289
	1321.609	367.87	39.10	27.07	47.55	7.7	N I	1199.549
	1322.751	722.81	47.30	31.88	57.04	12.7	N I	1200.223
	1323.596	127.75	28.70	17.51	33.62	3.8	N I	1200.709
	1329.819	577.04	69.92	52.79	87.62	6.6	Si III	1206.500
	1379.656	131.18	36.57	26.86	45.38	2.9	S II	1250.578
	1381.584	407.20	59.73	68.92	91.20	4.5	S II	1253.805
	1389.292	1661.66b	88.73	116.52	146.46	11.3	Si II	1260.422
	1394.919	204.98	43.83	40.08	59.39	3.5	Si II*	1264.737
	1435.556	898.99	58.77	55.16	80.60	11.2	O I	1302.168
	1437.779	1229.33	66.64	67.80	95.06	12.9	Si II	1304.370
	1471.121	1838.09b?	89.63	89.61	126.74	14.5	C II	1334.532
	1483.332	565.69n	79.24	111.92	137.13	4.1	Ni II	1345.878
	1536.460	328.43	56.89	47.79	74.30	4.4	Si IV	1393.760
	1683.181	612.38	98.75	71.69	122.03	5.0	Si II	1526.707

Table 2
(Continued)

Quasar	λ_{obs} (Å)	W_{obs}^1 (mÅ)	$\sigma W_{obs}^{phot,2}$ (mÅ)	$\sigma W_{obs}^{cont,3}$ (mÅ)	$\sigma W_{obs}^{tot,4}$ (mÅ)	$W^5/\sigma W_{tot}$	Ion	λ_{rest}
	1706.528	720.49	87.82	55.00	103.62	7.0	C IV	1548.204
	1709.616	987.15b	103.52	77.54	129.34	7.6	C IV	1550.781
	1736.325	476.75	85.38	68.26	109.31	4.4	Co II	1574.550
	1841.708	604.02	145.91	108.05	181.56	3.3	Al II	1670.788
	1885.903	587.57	133.69	43.12	140.47	4.2	Ni II	1709.604
	1919.265	370.32	113.36	57.81	127.25	2.9	Ni II	1741.553
	1931.124	1154.98b?	171.78	90.21	194.03	6.0	Ni II	1751.915
Q1659+6202	1279.329	319.26	69.22	74.22	101.48	3.1	P II	1152.818
	1286.556	161.43	39.97	40.11	56.63	2.9	C I	1157.909
	1321.172	307.83b?	24.86	14.33	28.70	10.7	S III	1190.203
	1321.740	346.17b?	28.30	20.23	34.79	10.0	Si II	1190.415
	1324.864	735.41	40.82	41.56	58.25	12.6	Si II	1193.289
	1333.011	1793.01b	55.63	58.78	80.93	22.2	N I	1199.549
	1388.469	226.62	30.68	27.37	41.12	5.5	S II	1250.578
	1391.981	225.09	31.78	29.89	43.62	5.2	S II	1253.805
	1398.352	194.98b?	25.94	18.52	31.87	6.1	S II	1259.518
	1399.428	1040.39b?	44.21	38.76	58.80	17.7	Si II	1260.422
	1445.627	881.06	37.19	40.96	55.33	15.9	O I	1302.168
	1448.062	639.13	35.41	41.14	54.28	11.8	Si II	1304.370
	1481.908	1500.84	33.78	37.98	50.83	29.5	C II	1334.532
	1463.251	620.76	37.42	55.90	67.27	9.2	Ni II	1317.217
	1495.086	209.77	18.51	20.80	27.85	7.5	Ni II	1345.878
	1521.052	198.26	24.26	26.54	35.96	5.5	Ni II	1370.132
	1547.135	591.20b?	35.98	31.72	47.97	12.3	Si IV	1393.760
	1557.247	307.65	34.22	35.53	49.33	6.2	Si IV	1402.772
Q2117-0026	1146.336	550.65	110.70	69.39	130.65	4.2	N II	1083.993
	1262.129	1064.35b	104.44	94.70	140.98	7.5	Si II	1193.289
	1269.541	1133.87b	112.84	118.35	163.52	6.9	N I	1200.223
	1310.159	138.09	54.34	51.00	74.52	1.9	N V	1238.821
	1315.415	433.45b	62.11	52.07	81.05	5.3	N V	1242.804
	1323.359	505.95b	85.84	89.36	123.92	4.1	S II	1250.578
	1326.531	717.25b	85.84	74.87	113.90	6.3	S II	1253.805
	1332.281	378.27	66.96	49.58	83.31	4.5	S II	1259.518
	1333.463	663.46	71.57	40.79	82.38	8.1	Si II	1260.422
	1377.631	401.40	89.00	81.67	120.79	3.3	O I	1302.168
	1380.075	348.15	69.62	41.62	81.11	4.3	Si II	1304.370
	1412.108	1152.08	126.92	131.81	182.98	6.3	C II	1334.532
	1411.955	958.22	107.27	83.01	135.64	7.1	C II	1334.532
	1474.881	807.27	113.97	110.91	159.03	5.1	Si IV	1393.760
	1483.744	582.64	116.09	136.46	179.16	3.3	Si IV	1402.772
	1615.124	924.61b	125.58	83.16	150.62	6.1	Si II	1526.707
	1637.733	1084.52	154.45	162.22	223.99	4.8	C IV	1548.204
	1639.857	654.51	129.79	125.83	180.77	3.6	C IV	1550.781

Note. 1. Observed-frame equivalent width in milliangstroms. A "b" or "b?" after the equivalent width value denotes a blend or a possible blend with another unrelated absorption feature. 2. 1σ uncertainty in the measured equivalent width in milliangstroms due to photon noise. 3. 1σ uncertainty in the measured equivalent width in milliangstroms due to uncertainty in continuum determination. 4. Combined 1σ uncertainty in the measured equivalent width in milliangstroms. 5 Significance level of the absorption feature.

Joshi et al. 2017). However, the DLA troughs for our absorbers do not show significant Lyα emission.

Table 3 lists the physical area probed by the COS aperture and the SDSS aperture at the redshift of the galaxy. It is possible that the Lyα emission from our galaxies is spatially offset from the regions covered by the COS aperture. We note in this context that, in the local universe, strong offsets between Lyα emission locations and stellar light locations have been observed (Kunth et al. 2003; Hayes et al. 2005; Östlin et al. 2009). Furthermore, Wisotzki et al. (2016) showed that galaxies at $3 < z < 6$ have diffuse Lyα emission halos with scale lengths of up to ~7 kpc, and that between 40% and 90% of the total Lyα flux comes from the extended halo. Obtaining

UV imaging of our galaxy sample may show that Lyα emission is extended and diffuse rather than concentrated within the instrument aperture due to the scattered nature of the emission line.

4. H I 21 cm Emission

Observations were carried out for five out of our 10 quasar sight lines with the GBT (PID AGBT16B_033, PI: N. Gupta), in order to determine the H I gas masses of the absorbing galaxies. The observations were carried out using the GBT's Gregorian focus *L*-band receiver and were spread over eight observing runs during 2016 August–October (see Table 4). The

Table 3
COS Absorption Characteristics

Quasar	log N_{HI} (cm^{-2})	Δv^1 (km s^{-1})	A_{COS}^3 (pkpc^2)	A_{SDSS}^4 (pkpc^2)
Q0902+1414[2]	...	...	5	7
Q1005+5302	$20.08^{+0.08}_{-0.07}$	$-131.5^{+9.8}_{-7.9}$	28	41
Q1010-0100	$21.38^{+0.07}_{-0.07}$	$-185.0^{+29.0}_{-29.0}$	1	2
Q1130+6026	$20.57^{+0.04}_{-0.04}$	$-65.0^{+8.0}_{-8.0}$	7	10
Q1135+2414	$20.57^{+0.03}_{-0.03}$	$11.0^{+8.0}_{-8.0}$	3	3
Q1328+2159	$21.01^{+0.11}_{-0.11}$	$88.0^{+61.0}_{-46.0}$	28	41
Q1452+5443	$20.66^{+0.04}_{-0.03}$	$-137.0^{+6.0}_{-6.0}$	18	25
Q1457+5321[2]	...	...	8	12
Q1659+6202	$21.20^{+0.07}_{-0.05}$	$-4.0^{+10.0}_{-10.0}$	20	30
Q2117-0026	$21.35^{+0.07}_{-0.06}$	$-51.0^{+48.0}_{-37.0}$	6	9

Note. 1. Velocity offset of the absorption system relative to the galactic emission redshift (determined from nebular emission lines in SDSS spectra; see Figures 3 and 4). 2. Two sight lines from our sample had no detectable flux from the quasar, indicating the presence of higher-redshift LLSs. See the text for more details. 3. The physical area probed by the COS aperture at the galactic redshift. 4. The physical area probed by the SDSS aperture at the galactic redshift.

Table 4
H I 21 cm Emission Measurements

Quasar	z_{gal}	z_{abs}	Run ID	rms (mJy)	M_{HI} ($10^9 M_\odot$)
J1010-0100	0.0213	0.02067	3	1.28	<0.36
J1130+6026	0.0604	0.06017	1, 2	0.73	<1.72
J1135+2414	0.0343	0.03434	4	0.83	4.1
J1452+5443	0.1026	0.10210	4, 5, 7	3.64	<25.0
J1457+5321	0.0660	...[a]	6	0.56	12.6

Note.
[a] DLA could not be covered due to the presence of a higher-redshift Lyman-limit system.

VErsatile GBT Astronomical Spectrometer was used as the backend. A bandwidth of 11.720 MHz centered at the expected redshifted H I 21 cm line frequency was used. The band was split into 32,768 frequency channels. The data were acquired in two linear polarization channels, XX and YY, using a fast time sampling of 2 s. The observations were performed in standard position-switching mode with 2 minutes spent on-source and another 2 minutes off-source.

The data were processed based on NRAO's GBTIDL package following the procedures described in Gupta et al. (2012). First, the data were visually examined to identify and exclude scans with bad time stamps. After this, each scan was calibrated individually, and a first-order baseline was fitted and subtracted to remove residual calibration and bandpass errors. The spectra from individual scans of the target source from all of the observing runs were then combined to get the average XX and YY spectra. The XX and YY spectra were then combined to obtain the final stokes-I spectra. The corresponding spectral rms (1σ) values are provided in Column 5 of Table 4.

The H I 21 cm emission is detected in two cases, i.e., the $z = 0.0343$ galaxy toward Q1135+2414 and the $z = 0.0660$ galaxy toward Q1457+5321. In both cases, the broad H I 21
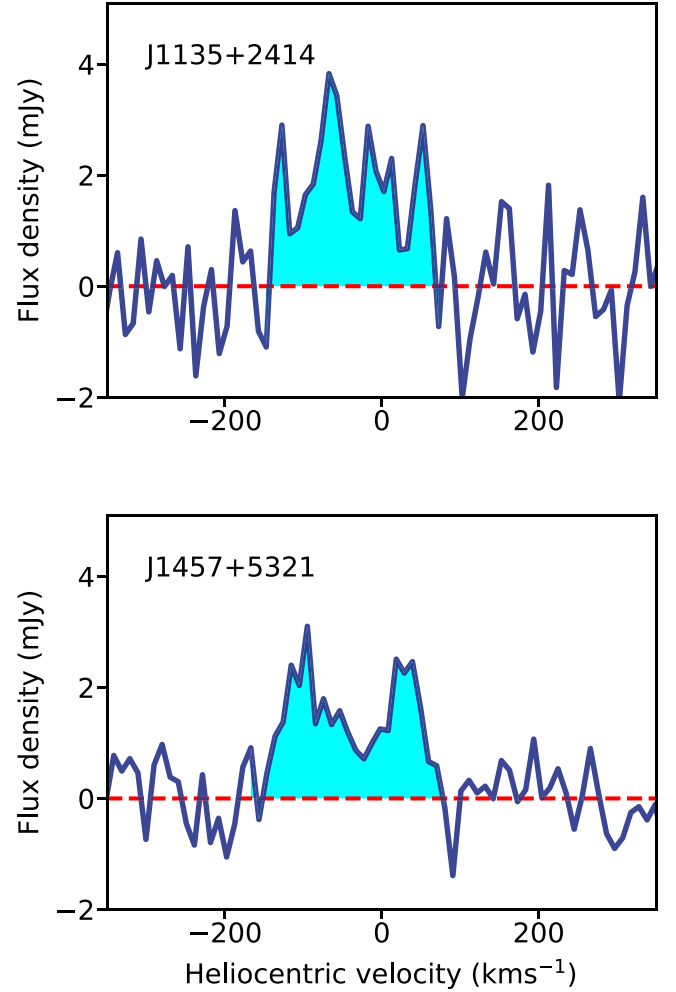

Figure 5. GBT spectra for two of our GOTOQs showing detections of H I 21 cm emission (highlighted in cyan). The velocities are with respect to $z = 0.0343$ and $z = 0.0660$, respectively, for Q11135+2414 and Q1457+5321.

cm emission detections are somewhat offset with respect to the galactic redshifts (the latter based on nebular emission lines), by $\sim$130–150 km s^{-1}. Figure 5 shows these detections. The spectra presented in the figure have been smoothed to a spectral resolution of $\sim$20 km s^{-1}. The integrated line fluxes $\int S dv$ in these cases are 0.79 and 0.64 Jy km s^{-1}, respectively. Following the procedure outlined in Gupta et al. (2018), the corresponding total H I masses are estimated using the relation

$$M_{HI} = 2.356 \times 10^5 \frac{D_L^2}{(1+z)} \int S dv. \quad (3)$$

The total H I masses thus estimated are summarized in Column 6 of Table 4. For the three nondetections, 3σ upper limits on the H I mass, derived assuming an intrinsic emission line width of 100 km s^{-1}, are listed.

Interestingly, the GOTOQs with H I 21 cm emission detections are in the sight lines to two of the top three most reddened background quasars in our sample of 10 GOTOQs [$E(B-V) = 0.36$ and 0.39, respectively, for Q1135+2414 and Q1457+5321]. On the other hand, no 21 cm emission is detected at $z = 0.02$ in the field of Q1010-0100, while the Hα/Hβ emission line ratio indicates a considerably larger amount of dust [$E(B-V) = 1.16$] than the GOTOQs in the fields of Q1135+2414 or Q1457+5321; this indicates substantial

variation in the 21 cm emission to the $E(B - V)$ ratio. It will be interesting to obtain H I 21 cm emission measurements for a large sample of GOTOQs to examine whether such variations are common.

5. Discussion

We now present the statistics of our H I detections, and discuss our sample in comparison with the literature, examining the correlations among the various galaxy and absorber properties.

5.1. H I Column Densities and Velocity Offsets in Our Sample

The H I column densities for the absorbers in our sample are found to be in the range of log $N_{HI} = 20.08^{+0.08}_{-0.07}$ to 21.38 ± 0.07 in all eight cases where the FUV flux of the quasar was detectable in the wavelength region near the Lyα absorption line at the GOTOQ redshift. Thus, our study has a 100% success rate in detecting new DLA/sub-DLAs. The 50% fraction of DLAs with log $N_{HI} \geqslant 21.0$ seems higher than may be expected based on the H I column density distribution of higher-redshift DLAs. But we caution that such comparisons may not be meaningful both because the GOTOQ sample is small, and because the selection strategies are very different for the GOTOQ sample (based on the galaxy) and the general DLA population (based on the absorber).

The velocity offsets of the absorption redshifts of the detected systems (as determined from the DLA fits) compared to the redshifts of the galaxies (determined from nebular emission lines) has a mean of -26.4 km s^{-1} with a standard deviation of 106.5 km s^{-1}. (The large standard deviation reflects the fact that the velocity offset is much larger, ranging in absolute value from 88 to 185 km s^{-1}, for four of the eight GOTOQs with detected DLA/sub-DLAs). We note that given the low resolution of the COS G140L spectra ($\sim$200 km s^{-1} at $\sim$1350 Å), it is not possible to determine the metal-line velocity profiles accurately; therefore, we cannot use the metal lines to determine the absorption redshifts. We note, however, that the absorption redshifts determined from the DLA profiles match closely with those determined from the Na I and Ca II absorption lines, in the few cases where these lines are detected in the SDSS spectra. We therefore adopt the redshifts estimated from the DLA fits, and caution that higher-resolution spectra are needed to determine the metal absorption redshifts more accurately. We also note that the redshifts of the galaxies based on the nebular emission lines detected in the quasar spectra are measured away from the galaxy centers, at impact parameters ranging from 1.2 to 7.2 kpc. In any case, the offset values between the absorber redshifts from the DLA fits and the galactic redshifts are well within the range of velocity spreads generally observed for DLA/sub-DLAs in higher-resolution spectroscopy, and there is little doubt that the detected absorbers are associated with the respective galaxies (or intervening cluster of galaxy-like objects at similar redshifts).

5.2. H I Column Densities and Reddening of the Background Quasars

It is also of interest to examine how the H I column densities and the dust in the absorbing galaxies correlate. One potential way to assess the dust content is via the reddening $E(B - V)$ of the background quasar. The ratio of the H I column density and reddening $N_{HI}/E(B - V)$ for the GOTOQ toward Q1135+2414

is 1.03×10^{21}, far below the ratio of the total H column density to reddening $N_H/E(B - V) = 5.8 \times 10^{21}$ observed in the Milky Way (Savage et al. 1977; Bohlin et al. 1978), possibly suggesting a predominance of H_2 in this sight line. In fact, only two of the eight sight lines with N_{HI} measurements in our HST COS sample are consistent with even the nonlinear trend between $N_{HI}/5.8 \times 10^{21}$ and $E(B - V)$ observed in the Milky Way ISM (e.g., Lizst 2014): four of the sight lines lie far above the Milky Way trend, and two others lie significantly below it. Part of the reason for the variation may be that the H I column density and the reddening considered here correspond to different ISM phases. The H I column densities are determined from Lyα absorption in the quasar sight line, and trace predominantly neutral gas (e.g., Viegas 1995; Vladilo et al. 2001; Péroux et al. 2007). On the other hand, the $E(B - V)$ values are estimated from the flux ratios of the Hα and Hβ recombination emission lines (detected in the SDSS spectra for our GOTOQs; see Section 2.2.2), which arise in the ionized gas in the star-forming regions (Straka et al. 2015). Thus, a perfect correlation between N_{HI} and $E(B - V)$ need not exist. Furthermore, a scatter in the metallicity and in the composition and size distribution of dust grains can also give rise to a lack of correlation between N_{HI} and $E(B - V)$ (see, e.g., Ledoux et al. 2015).

5.3. Comparison Sample from the Literature

We now combine our sample with the literature to search for trends between various galaxy and absorber properties, i.e., the impact parameter ρ, r-band luminosity relative to L_*, SFR, stellar mass, H I column density, absorber redshift, and velocity offset Δv between the absorber and the galaxy, against each other (assuming the observed, intervening galaxies are the only ones contributing). For this purpose, we have compiled a comparison sample of spectroscopically confirmed galaxies detected at the same redshifts as DLA/sub-DLA absorbers based on the available measurements from the literature (Bowen et al. 2005; Christensen et al. 2005; Zwaan et al. 2005; Rosenberg et al. 2006; Péroux et al. 2011; Noterdaeme et al. 2012a; Battisti et al. 2012; Fynbo et al. 2013; Christensen et al. 2014; Som et al. 2015; Péroux et al. 2016; Srianand et al. 2016; Krogager et al. 2017; Neeleman et al. 2017; Péroux et al. 2017; Zafar et al. 2017; Augustin et al. 2018; Kanekar et al. 2018; Ma et al. 2018; Rahmani et al. 2018; Rhodin et al. 2018; Borthakur et al. 2019; Frye et al. 2019; Mackenzie et al. 2019; Neeleman et al. 2019; Péroux et al. 2019; Hamanowicz et al. 2020; Kanekar et al. 2020; Neeleman et al. 2020; Ranjan et al. 2020; Dupuis et al. 2021; Joshi et al. 2021; Kaur et al. 2021; Rhodin et al. 2021, and references therein). The candidate galaxies for the $z = 0.0912$ DLA in O I 363 and the $z = 0.0063$ DLA in PG 1216+069 have been excluded because they have not been spectroscopically confirmed, and no impact parameter is known for them. The $z = 2.412$ absorber toward Q0918 +1636 was excluded because it has no continuum detection, and an emission line detection of only [O III] λ5007, which is known to be a poor indicator of SFR (e.g., Kennicutt 1992; Moustakas et al. 2006). The full sample, including our GOTOQ sample, consists of 117 galaxies at redshifts $0 < z < 4.4$ believed to be associated with DLA/sub-DLA absorbers (either as the primary absorbing galaxies, or as members of the same group of galaxies).

We note that about 39% of the galaxies in this full sample (46 out of 117) are cases where multiple galaxies are detected

at the redshift of the same DLA/sub-DLA (Christensen et al. 2005; Péroux et al. 2011; Battisti et al. 2012; Christensen et al. 2014; Péroux et al. 2016; Augustin et al. 2018; Borthakur et al. 2019; Frye et al. 2019; Mackenzie et al. 2019; Neeleman et al. 2019; Péroux et al. 2019; Hamanowicz et al. 2020; Kaur et al. 2021). In such cases, if the individual galaxies had measurements of luminosity, stellar mass, and/or SFR, we counted them individually. If only a combined luminosity, stellar mass, and/or SFR was known, the combined measurement was treated as a single object. This approach allows us to maximize the sample while searching for trends between the different stellar properties of the galaxies found in the fields of absorbers. (We note that most of the quantities presented in our examination of correlations in Section 5.5 below are galactic properties, not absorber properties.)

5.4. Stellar Properties of the Galaxies

5.4.1. Galaxies in Our Sample

The mean impact parameter of the galaxy center from the quasar sight line for our GOTOQ sample is 4.1 kpc with a standard deviation of 1.8 kpc. All galaxies are within projected separations of $\leqslant 7.2$ kpc from the corresponding quasars. We note that the GOTOQ sample has small impact parameters by construction, since the galaxies were found by searching for emission lines in the SDSS fiber. We note that the $3''$ diameter of the SDSS fibers corresponds to an impact parameter of 1.8 kpc at the median redshift of our sample (with a range of 0.65–3.6 kpc for our full sample).

The stellar masses of all of the galaxies from our sample are adopted from Straka et al. (2015). These M^* values are based on fitting of SEDs constructed using the available photometry in the five SDSS bands, using the photometric redshift code HYPERZ (Bolzonella et al. 2000). HYPERZ uses the stellar population synthesis models of Bruzual & Charlot (2003) and minimizes the reduced χ^2 to compute the best-fitting SED. The SFRs of our galaxies are based on measurements of the Hα and [O II] $\lambda3727$ emission lines (Straka et al. 2015), corrected by those authors for dust extinction using the Hα/Hβ line ratio, and corrected for fiber losses using the approximate approach explained in Section 2.2.2. The average SFR for our GOTOQ sample is 1.0 $M_\odot$ yr^{-1} with a standard deviation of 1.4 $M_\odot$ yr^{-1}. Follow-up high-resolution multiband imaging or integral field spectroscopy is necessary for us to understand the global stellar population and star formation history (SFH) of these galaxies.

5.4.2. Galaxies in the Comparison Sample

For a substantial fraction of the galaxies from the comparison sample, the stellar masses are direct measurements based on SED fitting of the galaxies. In the remaining cases where the stellar mass based on SED fitting was not available, if the SFR was available, M^* was estimated from the SFR based on the redshift evolution of the star-forming main sequence, as parameterized by Boogaard et al. (2018) for $0 < z < 0.5$,[11] and by Whitaker et al. (2014, 2020) for $0.5 < z < 2.5$[12], and adopting the latter for $z > 2.5$ as well. If neither SED-fitting

results nor the SFR were available, M^* was estimated from the luminosity. To do this, we used an empirical calibration log $(M^*/M_\odot) = 1.13$ log $(L/L_*) + 9.85$, based on a linear regression between log (L/L_*) and log M^* for all 23 galaxies in our sample (including all of our GOTOQs and 13 absorbing galaxies from the literature) for which independent estimates of the stellar mass and the luminosity were available. (See Section 5.5 and Figure 7 below for more discussion of how well the stated relations fit the observed data for DLA/sub-DLA galaxies.)

In total, we have stellar mass estimates for ∼86% of our full sample. We consider the values from SED fitting (available for ∼54% of our sample) as more reliable, and regard the rest as indicative. While searching for trends between the various parameters, we present statistics for both the subset with stellar mass values based on SED fitting ($M^*_{\rm SED}$) and the overall set including the stellar mass values based on SFR or luminosity ($M^*_{\rm adopt}$).

5.5. Correlations among Galaxy and Absorber Properties

We now combine our GOTOQ sample with the literature sample in an attempt to search for trends between the various galaxy and absorber properties, since both of these samples are ultimately cases of galaxies and absorbers associated with each other. Of course, we note that these two samples were selected in different ways, with the GOTOQ sample being galaxy-selected, and the literature sample being primarily absorber-selected. Furthermore, due to the requirement to have detectable emission lines in the SDSS fiber, the GOTOQ sample selects galaxies that are star-forming, at least to some extent; the literature sample has no such constraint. A more direct comparison using uniform selection criteria and covering the whole multidimensional parameter space (in redshift, impact parameter, stellar mass, luminosity, SFR, etc.) would of course be ideal, but the currently available samples do not allow that. Furthermore, we emphasize that we are not looking at how populated the different regions of the parameter space are, but merely at whether there are any trends between the various parameters. We also note that even within the literature sample, different studies differ in measurement techniques (e.g., narrowband imaging, long-slit spectroscopy, or integral field spectroscopy) and in the rest-frame wavelength regions used for observing the absorber galaxies (e.g., optical or far-infrared/submillimeter). Indeed, in a few of the cases where both rest-frame UV and far-IR data exist, the SFRs based on far-IR (e.g., the continuum near [C II] 158 μm emission) observations have been found to be higher than those based on the near-UV continuum, indicating the presence of some dust extinction, though in general dust extinction seems to be relatively modest (e.g., Kaur et al. 2021).

Figure 6 shows the H I column densities and absorption redshifts of the DLAs/sub-DLAs detected in this study and those at $z_{\rm abs} < 0.35$ from the literature. The Spearman rank order correlation coefficient is $r_S = -0.132$ with a high two-tailed probability $P = 0.528$ that this value of r_S arises purely by chance. Thus, no significant correlation is observed between $N_{\rm HI}$ and $z_{\rm abs}$ at $z_{\rm abs} < 0.35$.

The top panel of Figure 7 shows the stellar mass based on SED fitting versus SFR for all 43 galaxies in our sample for which these measurements are available (including all of our GOTOQs and 33 other galaxies associated with DLA/sub-DLAs from the literature mentioned in Section 5.3). For comparison the SFMSs

---

[11] log SFR $= 0.83$ log $(M^*/10^{8.5}\,M_\odot) - 0.83 + 1.74$ log $([1+z]/1.55)$.
[12] log SFR $= a + b$ log $(M^*/M_\odot) + c$ [log $(M^*/M_\odot)]^2$, with the higher-precision values of the redshift-dependent coefficients a, b, and c tabulated in Whitaker et al. (2020).
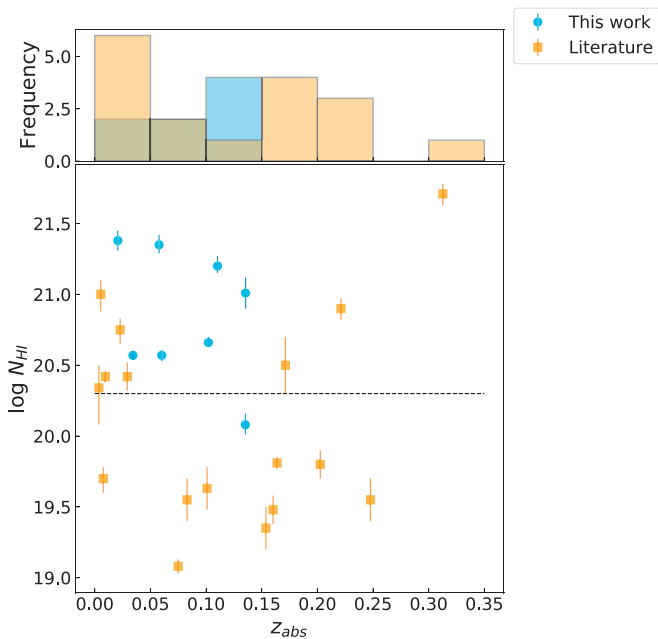
Figure 6. Top: redshift distribution of absorbers from this study and those with redshifts $z < 0.35$ from the literature. Bottom: H I column density vs. absorption redshift for absorbers from our study and those with redshifts $z < 0.35$ from the literature. For reference, the horizontal dashed line shows the boundary between DLAs and sub-DLAs.

of Boogaard et al. (2018) and Whitaker et al. (2014) are also shown. A substantial fraction of DLA/sub-DLA galaxies appear to be generally consistent with the SFMS trends for galaxies. Indeed, this also justifies our use of these relations for estimating the stellar masses of some other galaxies for which SED fitting was not available but SFR measurements were available. The bottom panel of Figure 7 shows the stellar mass based on SED fitting versus luminosity data for all 23 galaxies in our sample for which these measurements are available (including all of our GOTOQs and 13 other galaxies associated with DLA/sub-DLAs from the literature). Also shown is our best fit based on linear regression (mentioned above in Section 5.4.2). Overall, this appears to be a good fit to the available data, justifying our use of this relation to estimate stellar masses for some other galaxies where neither SED-fitting results nor the SFR were available.

Figure 8 shows plots of various properties of the full sample to examine correlations. The cyan circles denote the GOTOQs from this work, while the orange squares denote the measurements from the literature. Table 5 shows the results of correlation tests between the various parameters of interest, listing the Spearman rank order correlation coefficient r_S between pairs of parameters, and the corresponding probability of the observed value of r_S occurring purely by chance. A number of statistically significant correlations (with a <0.05 probability of occurring purely by chance, i.e., without the existence of an underlying correlation) are evident in many of the panels of Figure 8. We discuss these trends and their potential implications below.

A positive correlation is observed between the stellar mass and impact parameter (as seen in the second panel from the left in the fourth row from the top in Figure 8). This may potentially indicate that more massive galaxies can have gas-rich regions detectable as DLA/sub-DLAs out to larger galactocentric distances. Indeed, the "size of an H I disk" (defined as the radius at which the H I column density is

1.25×10^{20} cm^{-2}) is known to correlate strongly with the H I mass (e.g., Cimatti et al. 2020). The H I mass and stellar mass for late-type galaxies are also well-correlated (e.g., see Calette et al. 2018, and Section 5.5.6 below). Thus, a positive trend is indeed present between the H I sizes and stellar masses of late-type galaxies: $\log(R_{\rm H\,I}/10 \text{ kpc}) \approx 0.29 \log(M^*/M_\odot)$–2.77. Our finding of a positive correlation between stellar masses of galaxies and impact parameters to background quasars showing DLA/sub-DLAs at the galactic redshifts would also be supported by cosmological hydrodynamical simulations (e.g., Ford et al. 2013), which find that the extent of the regions with H I column densities in the DLA/sub-DLA range increases with the halo mass (which in turn is correlated positively with stellar mass, e.g., Mitchell et al. 2016; Girelli et al. 2020). Thus, more massive galaxies would be expected to have deeper gravitational potential wells that would allow them to hold on to neutral gas extending farther away from the center. The larger masses could potentially result from more pronounced galactic interactions, in line with recent suggestions that quasar absorbers may preferentially trace more overdense regions that would be expected to have more galactic interactions (e.g., Klitsch et al. 2019).

A positive correlation is also seen between luminosity and stellar mass (third panel from left in the fourth row from top in Figure 8), and between SFR and stellar mass (fourth panel from left in the fourth row from top in Figure 8). These latter relations arise partly because of the assumption of the SFMS or the observed stellar mass versus luminosity relation for estimating M^* values in some cases. We note that the M^* values in Figure 8 refer to the adopted stellar masses described earlier (including values derived from SED fitting or other techniques). However, as seen from Table 5, the trends between luminosity and M^* or between SFR and M^* remain strong even if only the M^* values derived directly from SED fitting are included. Overall, these positive correlations suggest that a substantial fraction of DLA/sub-DLA galaxies are generally consistent with the stellar mass–luminosity relation and the SFMS of star-forming galaxies. We return to a discussion of the SFMS in Section 5.5.5 below.

5.5.1. Trends in H I Column Density

We now consider trends between various galactic properties and the H I column density. In cases where multiple galaxies are detected at the redshift of the same DLA/sub-DLA, in principle, the contribution of each galaxy to the H I column density should be used. However, individual velocity components cannot be discerned in the Lyα absorption profiles (which are dominated by the broad damping wings). Higher Lyman series lines are not always covered, and even if they are, they can be blended with other Lyman forest lines, making it difficult to determine the velocity structure of the H I. It is thus not possible to determine H I column densities associated with the individual galaxies in cases where multiple galaxies are present at nearly the same redshift as the DLA/sub-DLA. Therefore, we use the same $N_{\rm HI}$ of the absorber for each galaxy associated with the absorber. (This is why there are some "horizontal lines" parallel to the $N_{\rm HI}$ axis in most of the panels in the lowest row of Figure 8 that show $\log N_{\rm HI}$ plotted versus the various other quantities.) We note that this is unavoidable with the existing data, and that this approach has also been adopted in other works in the literature (e.g., Hamanowicz et al. 2020).
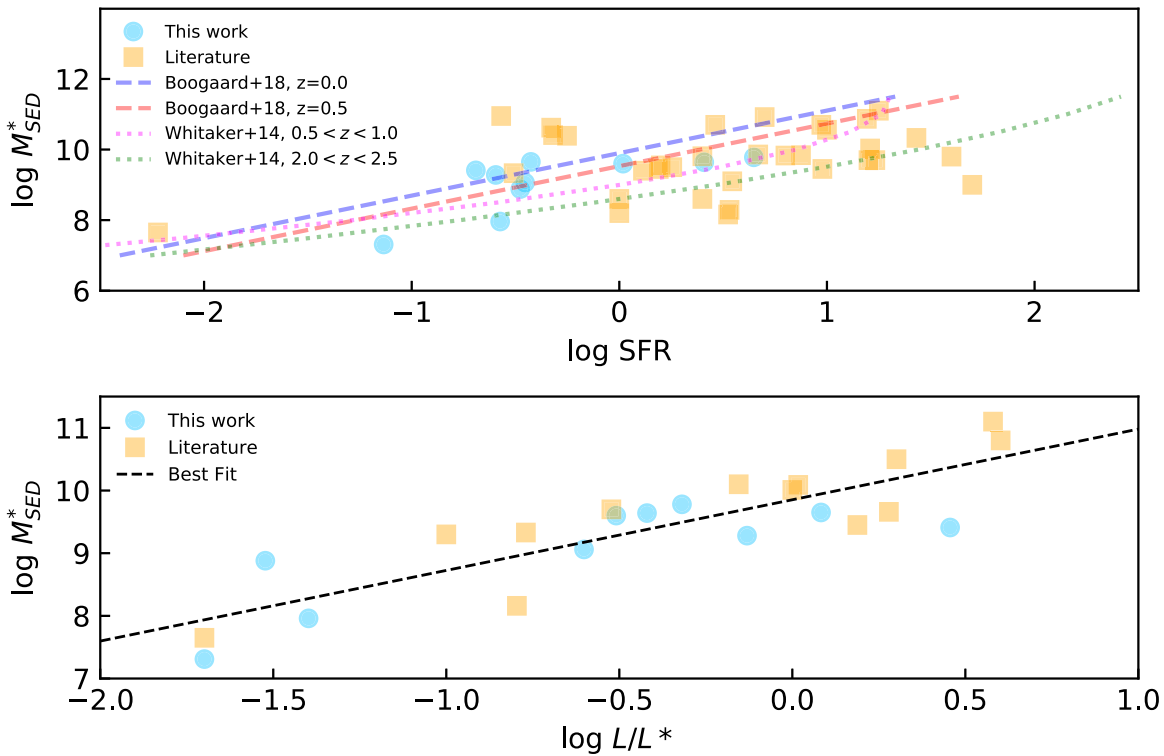
Figure 7. Top: stellar mass based on SED fitting vs. SFR measurements for galaxies associated with DLA/sub-DLAs. Cyan circles show GOTOQs from our sample, while orange squares show absorber–galaxy pairs from the literature. Dashed and dotted curves show, for comparison, the SFMS from Boogaard et al. (2018) and Whitaker et al. (2014) at a variety of redshifts. Bottom: stellar mass based on SED fitting vs. luminosity for galaxies associated with DLA/sub-DLAs. Cyan circles show GOTOQs from our sample, while orange squares show absorber–galaxy pairs from the literature. In both panels, some orange squares appear darker than others because of the overlap of multiple data points with similar values. The dashed black line shows our best fit based on linear regression. See the text for more details.

The H I column density shows a strong negative correlation with the impact parameter (as seen in the second panel from left in the bottom row of Figure 8). This trend becomes even stronger if only the distinct (nonduplicate) absorbers are considered, and the median impact parameter used in cases of multiple galaxies associated with the same absorber. A similar trend between absorption strength and impact parameter has been seen in smaller DLA samples before (e.g., Krogager et al. 2020) and for other types of absorbers such as Mg II absorbers (e.g., Nielsen et al. 2013; Huang et al. 2021). Our study is the first one to examine this trend in such a large sample focusing specifically on DLA/sub-DLAs. We also emphasize that our sample includes many absorbers at very low impact parameters. The decrease in H I column density with increasing impact parameter probably results from a decreasing probability of encountering high column density gas at increasing galactocentric radii. Our sample shows that the anticorrelation between the H I column density and impact parameter appears to extend even to the smallest impact parameters probed ($\lesssim 1$ kpc). Given the scatter in the data, it will be very interesting to increase the N_{HI} measurements at low impact parameters further and compare them to measurements for sight lines at larger impact parameters. Based on such comparisons, one can learn in a statistical sense about the variation in gas properties with galactocentric distance in the inner regions of galaxies, for example the radial gradients in H I column density and eventually in metallicity, and the redshift evolution of these gradients.

We also note in this context that a weak anticorrelation has been noted between 21 cm absorption optical depth and the impact parameter in a study of galaxies in the fields of 21 cm

absorbers at $z \sim 0.3$ (Gupta et al. 2013; Dutta et al. 2017a), including some GOTOQs. Combining measurements of the 21 cm absorption optical depth with the H I column density derived from the Lyα absorption allows estimation of the spin temperature of the gas. It would therefore be interesting to study 21 cm absorption in a larger sample of GOTOQs and use the 21 cm and Lyα absorption measurements together in order to understand how the properties of the cold neutral medium in these galaxies correlate with the SFRs and stellar masses of the galaxies. We note, however, that such a 21 cm absorption survey is not feasible at present, since most of the quasars with GOTOQs are not bright enough in the radio for 21 cm spectroscopy.

Interestingly, as seen from Table 5, there is also a tentative negative correlation between the H I column density and the stellar mass determined from SED fitting.[13] This negative correlation appears counterintuitive if one assumes the H I column density to reflect the mass. There is however no basis for making such an assumption, since the H I column density pertains to the gas density integrated along the specific line of sight, and does not track the mass due to the unknown and

---

[13] A similar trend is not seen with M^*_{adopt}, i.e., if galaxies with stellar masses determined from other techniques are included. Even if the M^* values for multiple galaxies corresponding to a given absorber are added together and treated as one single galaxy, the combined M^*_{SED} values show a significant anticorrelation with N_{HI}, but the combined M^*_{adopt} values do not show such a trend. However, we note that the other stellar mass estimates included in M^*_{adopt} are less reliable than those based on SED fitting. Indeed, most of these other stellar mass estimates are based on SFR, which does not show much correlation with the H I column density. In any case, given that the stellar masses based on SED fitting are more reliable, we regard the negative correlation between N_{HI} and M^*_{SED} as likely to be real.
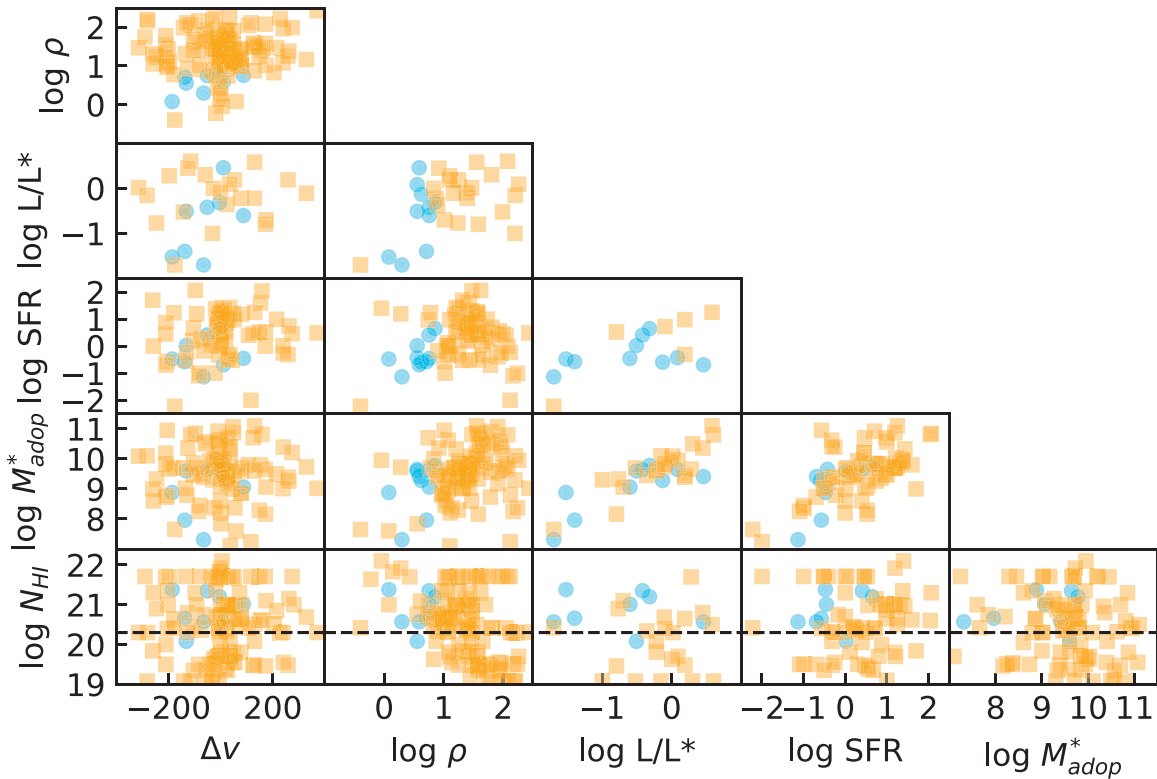
Figure 8. Various properties of galaxies associated with DLA/sub-DLA absorbers plotted against each other. Cyan circles show GOTOQs from our sample, while orange squares show absorber–galaxy pairs from the literature. Some orange squares appear darker than others because of the overlap of multiple data points with similar values. The dashed black lines in the lowest panels denote the separation in H I column density between DLAs and sub-DLAs. See the text for more details.

spatially nonuniform gas density and the unknown absorber geometry. Indeed, we note that a similar negative trend between the H I column density and the stellar mass was previously suggested in a much smaller sample (Augustin et al. 2018). Those authors also point out that most absorbers at $z \sim 1$ with $\log N_{HI} > 20.3$ have smaller stellar masses than the Milky Way. Earlier studies comparing DLA properties to those of local disk galaxies (e.g., Boissier et al. 2003; Zwaan et al. 2005) have also shown that low surface brightness galaxies contribute substantially to the number and H I mass of DLAs, and that 87% of the DLA cross section arises in sub-L^* galaxies. We also note in this context the suggestion in previous works that sub-DLAs may arise in higher-mass galaxies than DLAs (e.g., Khare et al. 2007; Kulkarni et al. 2010). The negative correlation we observe between N_{HI} and M^*_{SED} is consistent with this suggestion. We emphasize that this trend includes the full redshift range $0 < z < 4.4$, and is not limited to the low-z sub-DLAs whose high metallicities were partly the reason behind the suggestion of Khare et al. (2007) and Kulkarni et al. (2000).

5.5.2. Observed Dependence on Redshift

In Figure 9, we examine the observed trends in various properties with absorber redshift. There is a large "hole" in redshift space, which highlights the sparse coverage of absorbers in the range $1 \lesssim z \lesssim 1.8$. This sparse coverage highlights the difficulties in identifying galaxies associated with DLA/sub-DLAs at both low and high redshifts. At $z < 1.65$, the Lyα line (needed for determining the H I column density) lies in the UV, making it necessary to use HST to discover these DLA/sub-DLAs. The practical necessity to

target relatively bright quasars for UV spectroscopy with HST limits the number of DLA/sub-DLAs observed at $z < 1.65$. Furthermore, of the DLA/sub-DLAs detected in this redshift range, those at $z \lesssim 1$ are more easily identified with galaxies, since the latter are easier to image, making it easier to determine their stellar properties.

At $1.65 \lesssim z \lesssim 4.5$, the determination of H I column density is easier since the DLA/sub-DLA Lyα lines are redshifted into the optical range accessible to ground-based spectrographs. On the other hand, the imaging and spectroscopic confirmation of the absorbing galaxies is much harder due to the rapidly decreasing surface brightness of galaxies with increasing redshift, and due to the difficulty of spatially resolving the background quasar from the absorbing galaxy, which again limits the sample of DLA/sub-DLA galaxies. While great strides are being made in the imaging of galaxies associated with DLA/sub-DLAs using IFS, e.g., with Very Large Telescope MUSE and SINFONI (e.g., Péroux et al. 2011, 2016; Mackenzie et al. 2019; Péroux et al. 2019), the redshift ranges of the observed galaxies are limited by the wavelength coverage of the IFS for detecting nebular emission lines of the galaxies. The systems at $z > 3.8$ are based on Atacama Large Millimeter/submillimeter Array (ALMA) detections of [C II] 158 μm or CO (2–1) emission (e.g., Neeleman et al. 2017, 2019, 2020). We nevertheless attempt to understand the dependence on redshift of the absorbing galaxies using the data at higher and lower redshift, while emphasizing the need to increase the samples at all redshifts, and especially to fill the hole in the "redshift desert," given the importance of the epoch $1 < z < 2$ in the cosmic SFH.

The first and third panels from the top in Figure 9, showing galactic luminosities and stellar masses, respectively, do not

Table 5
Results of Correlation Tests between Galaxy and Absorber Parameters

Parameters	No. of Objects[1]	r_S[2]	P[3]	Figure, Panel[4]
Significant Correlations:				
z, $\log N_{\rm HI}$	85[5]	0.345	1.22×10^{-3}	9, 1, 5
z, $\log$ SFR	73	0.607	1.25×10^{-8}	9, 1, 2
$\log N_{\rm HI}$, $\log \rho$	113	-0.411	6.18×10^{-6}	8, 2, 5
$\log N_{\rm HI}$, $\log M_{\rm SED}^*$	59	-0.330	1.08×10^{-2}	...
$\log L/L_*$, $\log M_{\rm adopt}^*$	32	0.752	7.04×10^{-7}	8, 3, 4
$\log L/L_*$, $\log M_{\rm SED}^*$	23	0.791	6.95×10^{-6}	7, 1, 2
$\log L/L_*$, $\log$ SFR	16	0.526	3.65×10^{-2}	8, 3, 3
$\log \rho$, $\log M_{\rm adopt}^*$	97	0.271	7.35×10^{-3}	8, 2, 4
$\log \rho$, $\log M_{\rm SED}^*$	60	0.522	1.86×10^{-5}	...
$\log$ SFR, $\log M_{\rm adopt}^*$	73	0.575	1.05×10^{-7}	8, 4, 4
$\log$ SFR, $\log M_{\rm SED}^*$	43	0.445	2.81×10^{-3}	7, 1, 1
$\log$ sSFR, $\log (1 + z)$	43	0.452	2.33×10^{-3}	10, 1, 1
$\log$ sSFR, $\log M_{\rm SED}^*$	43	-0.548	1.42×10^{-4}	10, 1 , 2
Insignificant Correlations:				
z, $\log L/L_*$	32	0.269	0.137	9, 1, 1
z, $\log \rho$	115	0.0154	0.870	...
z, $\log M_{\rm adopt}^*$	98	0.144	0.158	9, 1, 3
z, $\log M_{\rm SED}^*$	61	0.157	0.228	...
z, Δv	115	0.116	0.215	9, 1, 4
$\log N_{\rm HI}$, $\log M_{\rm adopt}^*$	96	-0.158	0.125	8, 5, 5
$\log N_{\rm HI}$, $\log L/L_*$	30	-0.178	0.346	8, 3, 5
$\log N_{\rm HI}$, $\log$ SFR	71	0.0648	0.592	8, 4, 5
$\log N_{\rm HI}$, Δv	115	0.0315	0.739	8, 1, 5
$\log L/L_*$, $\log \rho$	32	0.347	0.0514	8, 2, 2
$\log L/L_*$, Δv	30	0.171	0.365	8, 1, 2
$\log M_{\rm adopt}^*$, Δv	96		-0.00525	0.960 8, 1, 4
$\log \rho$, $\log$ SFR	72	0.0592	0.622	8, 2, 3
$\log \rho$, Δv	113	0.0782	0.410	8, 1, 1
$\log$ SFR, Δv	71	0.183	0.126	8, 1, 3
$\log M_{\rm SED}^*$, Δv	59	0.0189	0.887	...

Note. 1. Number of galaxy–absorber pairs for which both parameters are available. 2. Spearman rank order correlation coefficient. 3. Probability that the observed value of r_S could arise purely by chance. 4. Figure and panel number showing the trend between the particular parameters. The first index denotes the figure number, the second index denotes the column number of the panel in that figure from the left, and the third index denotes the row number of the panel from the top of the entire figure. For Figures 7, 9, and 10, which contain only one column, we denote the column number as 1, i.e., counting multiple galaxies associated with the same absorber only once. 5. Correlation for nonduplicate objects (see the text for more details).

exhibit strong correlations in these quantities with respect to redshift. This reality underscores the fact that the absorption line technique used to identify most of the literature sample is independent of the galaxy's luminosity and mass.

Interesting trends are, however, seen in some of the remaining panels of Figure 9, despite the considerable scatter in the data. The second panel from the top shows the SFR of the galaxy plotted versus the redshift. A trend of SFR increasing with redshift is observed over the redshift range covered especially at $z \lesssim 1$. This suggests that the galaxies associated with DLAs and sub-DLAs (and those located in the same groups as the main absorbing galaxies) have SFHs consistent with the SFH of star-forming galaxies at least at

$z \lesssim 1$. The relatively flat SFR versus z trend at $z \gtrsim 2$ may appear a little surprising given that the global SFR density inferred from emission-based studies of star-forming galaxies shows a well-defined peak at $z \sim 2$ and a considerable decrease between $z \sim 2$ and $z \sim 4.5$ (e.g., Madau & Dickinson 2014). However, we note that the global trend does not reflect the SFR per galaxy, and the SFH of individual galaxies can differ considerably. Increasing the samples of galaxies associated with DLA/sub-DLAs at $z > 2$ will of course help to more accurately establish the redshift dependence trend at these redshifts. We discuss the SFH in more detail in Section 5.5.4 below.

The bottom panel in Figure 9 shows the H I column density plotted versus redshift for the full sample. The dashed black line in this panel denotes the separation between DLAs and sub-DLAs. Most of the sub-DLAs in the sample are at $z < 1.1$, while the DLAs cover the full range of redshifts. This may not be a physical effect, but a result of the fact that a much smaller number of sub-DLAs have been studied even in absorption at $z > 2$, and only a small minority of these have detections of the associated galaxies. This effect is probably responsible for the significant positive correlation observed between the H I column density and redshift in the absorbers associated with galaxies. (We note that the correlation between H I column density and redshift is evaluated only for "nonduplicate" objects, i.e., treating multiple galaxies detected at the same absorber redshift as one, since, as explained in Section 5.5.1, only the total H I column density is known and assigned to all of them.)

5.5.3. Gas Kinematics

The fourth panel from the top in Figure 9 shows the velocity offset Δv of the absorber relative to the galaxy versus the absorber redshift. For our GOTOQs, we use the centers of the H I Lyα profiles to determine the absorber redshifts. This is because the metal-line redshifts are not precisely known for the GOTOQs because of the very low resolution of the COS G140L grating that prevents accurate measurements of the metal-line profiles. The dashed black line in this panel separates the cases of absorbers at higher velocities with respect to the galaxies from those at lower velocities. No significant correlation is observed between Δv and redshift. Three-fourths of the absorbers (six out of eight) in our GOTOQ sample appear to be blueshifted ($\Delta v < 0$) with respect to the galaxies. However, the overall sample (including the comparison sample) shows a roughly equal incidence of positive and negative velocity offsets.

We caution that nonzero velocity offsets could arise partly from the fact that our absorption line measurements are based on the H I Lyα profiles measured in the COS G140L spectra. But given the low resolution and low S/N of these COS spectra, we do not consider it advisable to use the metal-line wavelengths as an indicator of the exact absorber redshift. We also note that the absorption redshifts we adopt from the H I Lyα lines agree well with those deduced from Ca II or Na I absorption lines in cases where the latter are detected in SDSS spectra. But high-resolution measurements of the metal lines are clearly essential for more accurate determinations of the absorber redshifts. If a dominance of absorbers with $\Delta v < 0$ persists in our GOTOQ sample even with high-resolution spectroscopy, and is confirmed in a larger GOTOQ sample, it
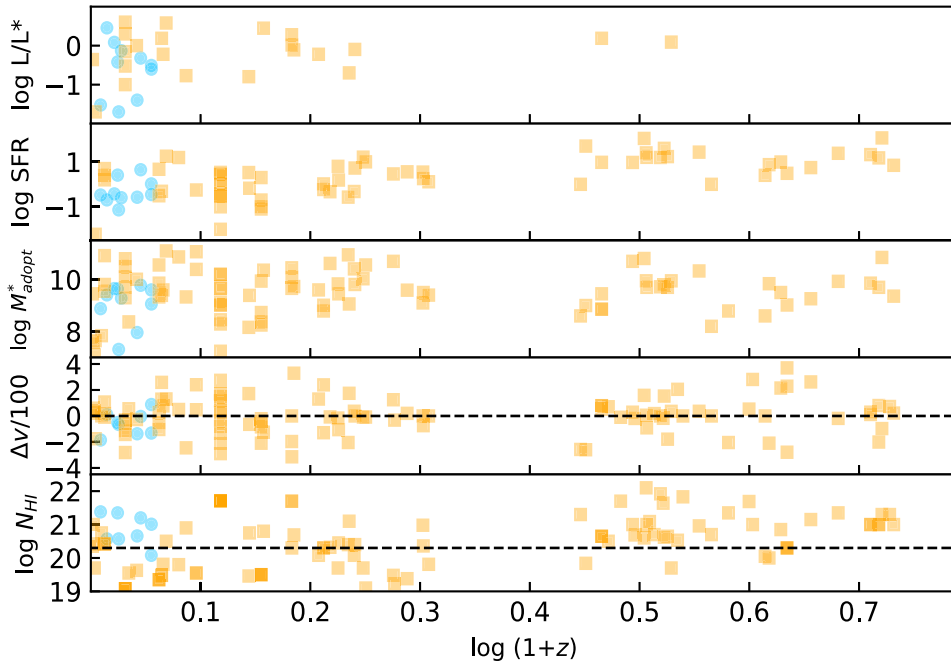
Figure 9. Trends in redshift of various galaxy and absorber properties. The panels show the luminosity, star formation rate, stellar mass of the galaxy, velocity offset of the absorber with respect to the galaxy, and the H I column density of the absorber plotted vs. redshift. Cyan circles show GOTOQs from our sample, while orange squares show galaxies from the literature. The dashed black line in the fourth panel from the top separates the cases of absorbers at higher redshifts with respect to the galaxies from those at lower redshifts. The dashed black line in the bottom panel denotes the separation in H I column density between DLAs and sub-DLAs. See the text for more details.

may provide further insights into the kinematics of the absorbing gas in the GOTOQs.

Absorption at $\Delta v < 0$ can occur in outflowing gas from the near side of a galaxy, or from inflowing gas on the far side of the galaxy, or from gas corotating with the disk of a galaxy. The galaxy's inclination and the orientation of the quasar sight line relative to the galaxy's major axis also matter in this context since, for example, gas outflows from galaxies are often believed to occur primarily along the minor axis, and gas inflows primarily along the major axis. Thus, negative velocity shifts could arise in outflows from the near side of a face-on galaxy or inflows on the far side of an edge-on galaxy, or in gas in the approaching side corotating with the disk of an edge-on galaxy. By contrast, positive velocity shifts can arise in outflows from the far side of a face-on galaxy or inflows on the near side of an edge-on galaxy, or in gas in the receding side corotating with the disk of an edge-on galaxy. Indeed, complex gas motions have been detected in some of the galaxies in our full sample based on integral field spectroscopy (e.g., Péroux et al. 2011, 2019). It will be interesting to sort out among the different possibilities for each individual case by combining the results from high-resolution spectroscopy of the background quasar with integral field spectroscopy of the foreground galaxy.

5.5.4. Star Formation History

Figure 10 examines in more detail the SFH for the galaxies in our full sample for which stellar mass estimates based on SED-fitting results are available. The upper panel shows the specific star formation rate ($\text{sSFR} = \text{SFR}/M^*_{\text{SED}}$) for the galaxies for which SED-fitting results are available, plotted versus redshift. While there is some scatter in the data points, there is an overall positive trend between sSFR and $\log(1 + z)$, with a Spearman rank order correlation coefficient of 0.452 and

a probability of 2.33×10^{-3} of this value of r_S occurring purely by chance. While the sample is small, the existing data suggest the existence of multiple sSFR versus redshift sequences, for galaxies of different stellar masses. This is consistent with the multiple sSFR versus redshift trends reported by Whitaker et al. (2014) for galaxies of different stellar masses. The dashed magenta and green curves show the sSFR versus redshift trends of Whitaker et al. (2014) for $\log M^* = 9.3$ and 11.1, respectively. The range in sSFR spanned by DLA/sub-DLA galaxies is larger. The existence of some DLA/sub-DLA galaxies with sSFRs above the curve for $\log M^* = 9.3$ is a result of some of the galaxies being lower in mass (as low as $\log M^* = 7.1$). However, it is surprising that some DLA/sub-DLA galaxies (∼20% of the galaxies plotted in Figure 10) lie below the curve for even $\log M^* = 11.1$, with the difference being substantial for ∼15%. Given that the stellar masses of these galaxies are in fact lower than $\log M^* = 11.1$, their low sSFRs suggest that their star formation activity is substantially below the expectations based on the SFMS. Some of these galaxies have stellar masses $10 < \log M^* < 11$ and moderately low SFRs, while some others have stellar masses $9 < \log M^* < 10$ and very low SFRs. In either case, these DLA/sub-DLAs are associated with galaxies with longer gas consumption timescales than the usual star-forming galaxies. This conclusion is consistent with the finding based on ALMA studies of molecular gas that some absorption-selected galaxies have extended gas disks (e.g., Klitsch et al. 2019). Such galaxies with larger cool gas reservoirs would be expected to take longer to consume the gas via star formation and have lower sSFRs.

5.5.5. Star Formation Main Sequence

The lower panel of Figure 10 shows the specific star formation rate versus the stellar mass for the galaxies in our full
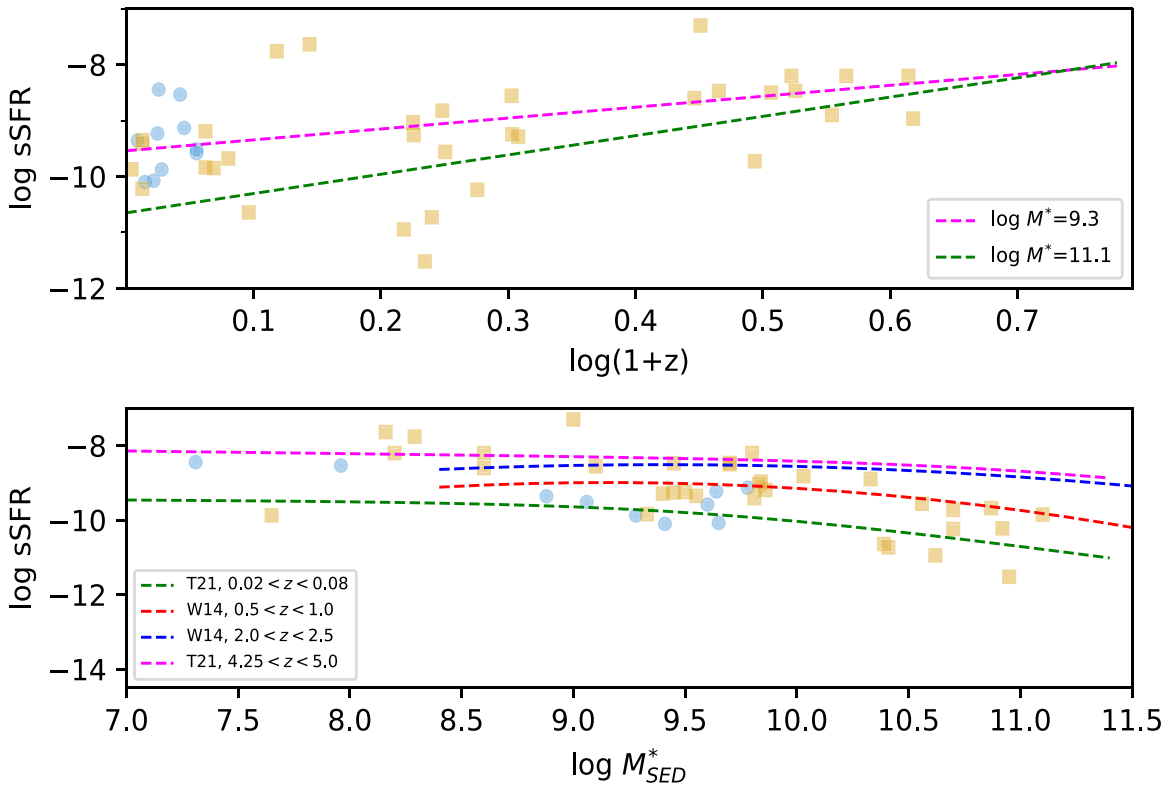
Figure 10. Specific star formation rate plotted vs. redshift (top panel), and vs. stellar mass (bottom panel) for DLA/sub-DLA galaxies that have stellar mass estimates from SED fitting. Cyan circles show GOTOQs from our sample, while orange squares show galaxies from the literature. Dashed curves in the upper panel show relations for star-forming galaxies for different stellar masses from Whitaker et al. (2014). Dashed curves in the lower panel show relations for star-forming galaxies for different redshift ranges from Whitaker et al. (2014) and Thorne et al. (2021). See the text for more details.

sample for which stellar mass estimates based on SED-fitting results are available. Once again, while there is considerable scatter, overall there is a significant negative correlation. The Spearman rank order correlation coefficient is -0.548 with a probability of 1.42×10^{-4} of this occurring purely by chance. The large scatter appears to result from different SFR versus stellar mass relations at different redshifts. The dashed red and blue curves show the SFMS for galaxies at $0.5 < z < 1.0$ and $2.0 < z < 2.5$ from Whitaker et al. (2014). The DLA/sub-DLA galaxies span a much wider range in sSFR and stellar mass than those covered in Whitaker et al. (2014), extending to stellar masses as low as $\log M^* = 7.1$. Furthermore, the DLA/sub-DLA sample covers a larger redshift range ($0 < z < 4.4$) than the range $0.5 < z < 2.5$ covered by Whitaker et al. (2014). For comparison, we also show the sSFR versus stellar mass relations determined by Thorne et al. (2021) that do extend down to lower masses and cover a wider redshift range. The green and magenta curves show the SFMS of Thorne et al. (2021) for the redshift ranges $0.02 < z < 0.08$ and $4.25 < z < 5.0$. These relations nicely bracket the range of sSFR covered by most DLA/sub-DLA galaxies. However, there are a few DLA/sub-DLA galaxies that have sSFRs below the range of the Thorne et al. (2021) relations. This may indicate the existence of some galaxies with lower star formation activity than expected from the SFMS for typical star-forming galaxies.

Thus, both panels of Figure 10 illustrate the power of the quasar absorption line technique to extend galactic evolution studies to low sSFRs and low stellar masses. Future studies of larger samples of DLA/sub-DLAs will help to grow this

population that may be missed by studies of emission-selected galaxies.

5.5.6. Gas Mass versus Stellar Mass

Figure 11 compares the H I gas mass and stellar mass for DLA/sub-DLA galaxies and local galaxies. The upper panel shows the H I mass versus stellar mass for the galaxies associated with DLAs/sub-DLAs from our study and the literature (Kanekar et al. 2018; Borthakur et al. 2019) for which stellar mass measurements exist, and H I 21 cm emission was searched for. Together, these consist of eight 21 cm detections and four upper limits in the redshift range of $0.01 \lesssim z \lesssim 0.10$. The detections (large blue circles) show a strong positive trend, with a Spearman rank order correlation coefficient of 0.952 and a probability of 2.60×10^{-4} of this value of r_S occurring purely by chance.

The remaining data points in Figure 11 show measurements for local ($0 < z < 0.03$) galaxies from the literature. These include galaxies from the THINGS survey (Leroy et al. 2008), the ALLSMOG survey (Bothwell et al. 2014), and a sample of gas-rich galaxies (McGaugh 2012). The DLA/sub-DLA data are seen to be overall consistent with the trends for local galaxies, with H I mass and stellar mass following the trend expected from the standard scaling relation. The dashed line shows the trend fitted by Calette et al. (2018) for late-type galaxies (LTGs; including spirals and irregulars). The DLA/sub-DLA galaxies lie above the LTG trend, extending to much lower stellar masses than the local spirals do, but fall in the general range of stellar masses for the gas-rich galaxies. While there is considerable scatter in the relation for both the
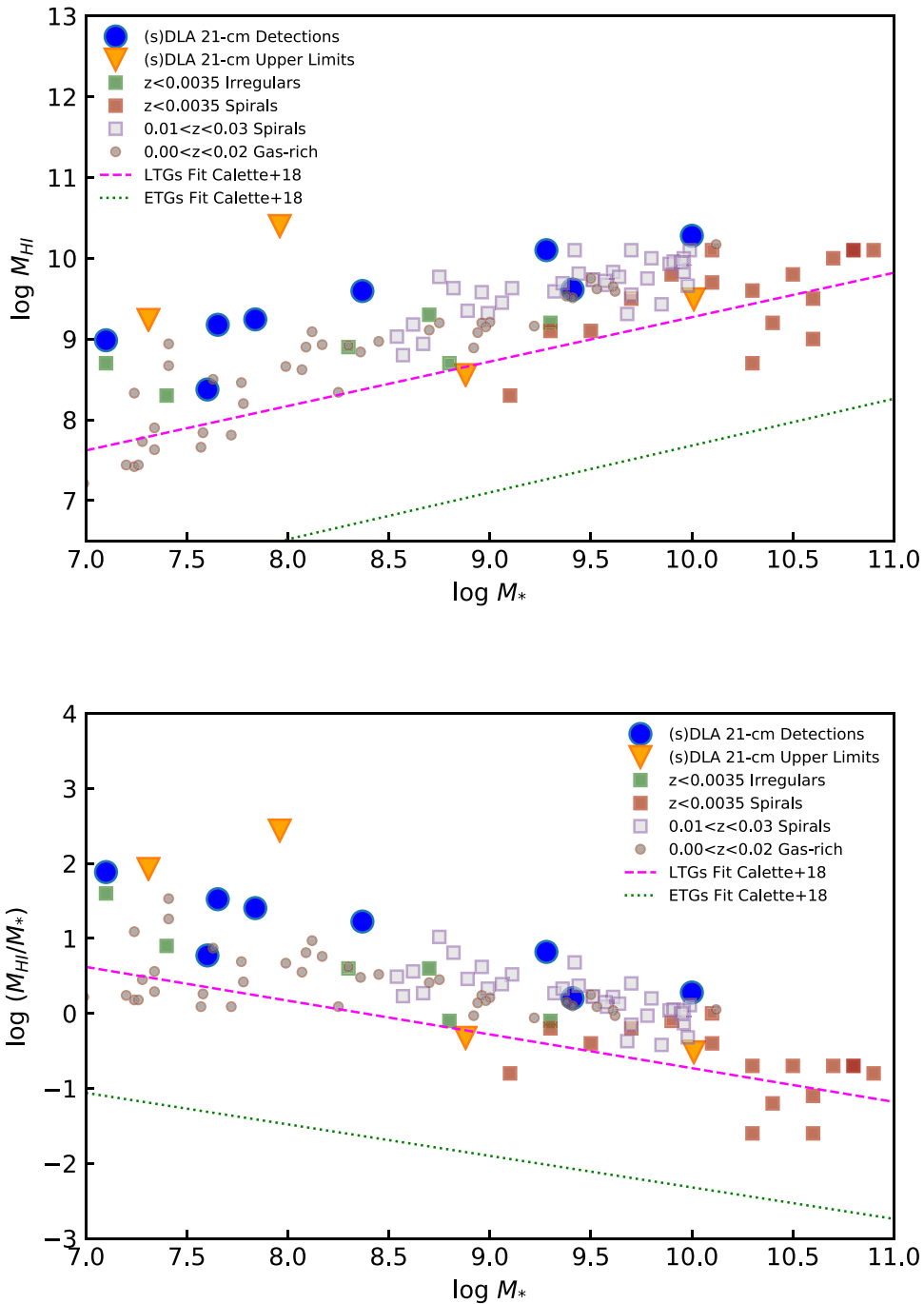
Figure 11. Top (a): H I gas mass vs. stellar mass for galaxies associated with DLA/sub-DLAs searched for in 21 cm emission from our sample and the literature. Other data points show H I and stellar masses of local spirals and irregulars, including gas-rich galaxies. The dashed and dotted lines show, respectively, the best-fitting trends found by Calette et al. (2018) for local late-type galaxies and early-type galaxies. Bottom (b): ratio of H I gas mass to stellar mass, plotted vs. stellar mass for galaxies associated with DLAs searched for in 21 cm emission from our sample and the literature. Symbols and lines have the same meaning as in the top panel. See the text for more details.

DLA/sub-DLA galaxies and the local galaxies, most (six of the eight) DLA/sub-DLA galaxies with 21 cm detections show a very tight relation, and lie at the upper end of the trends for the local galaxies, even the gas-rich local galaxies. In other words, most DLA/sub-DLA galaxies with 21 cm detections appear to have higher H I masses compared to the typical local galaxies with comparable stellar masses. This could potentially be an artifact of the small sample size; expanding the sample is thus essential to verify this trend.

The lower panel of Figure 11 shows the ratio of the H I mass to stellar mass for the DLA/sub-DLA galaxies and the comparison with values for local galaxies. The H I to stellar mass ratio falls off with increasing stellar mass for DLA/sub-DLA galaxies, as it does for local galaxies. However, the ratio is much higher for DLA/sub-DLA galaxies than for typical local spirals and irregulars. In fact, even at the low stellar masses, the H I mass to stellar mass ratio is higher for DLA/sub-DLA galaxies than for most of the gas-rich galaxies. This

is consistent with our suggestion that DLA/sub-DLAs trace galaxies with longer gas-depletion timescales than most star-forming galaxies. These suggestions are also consistent with the finding, based on observations of molecular gas, of larger gas-depletion times in H I-selected galaxies compared to emission-selected galaxies (e.g., Szakacs et al. 2021). It is essential to obtain H I 21 cm emission observations for a much larger DLA and sub-DLA sample to examine whether the trends seen in the DLA/sub-DLA sample presented here also hold for the overall DLA/sub-DLA population. It would also be very interesting to determine the gas mass to stellar mass ratio for higher-redshift DLA/sub-DLA galaxies and examine how this ratio has evolved with cosmic time. We note, however, that it has been shown to be extremely challenging to build up such a sample. Many more very low-redshift DLAs and sub-DLAs need to be identified to enable successful 21 cm observations.

The dotted lines in both panels of Figure 11 show the trend fitted by Calette et al. (2018) for early-type galaxies (ETGs). The DLA/sub-DLA galaxies lie far above the ETG trend, suggesting that most of the DLA galaxies with H I 21 cm detections (and possibly even those with 21 cm limits) are not ETGs. Of course, the existing DECaLS images of our GOTOQs (e.g., Figure 1) show that not all of our GOTOQs are obviously LTGs. However, these images are relatively shallow and low in spatial resolution. It is essential to obtain high-S/N and high-resolution images of the DLA/sub-DLA galaxies to determine the morphology more robustly and to assess whether the H I mass to stellar mass trends in these galaxies are consistent with the trends for local galaxies of different morphological types.

Figure 12 compares the H I gas masses and stellar masses of DLA/sub-DLA galaxies with nearby H I-selected galaxies. The upper panel shows the H I gas masses plotted versus stellar masses for the DLA/sub-DLA galaxies, along with the corresponding relation observed for galaxies selected by means of their H I emission, based on a sample of 9,153 H I-selected ALFALFA galaxies with SDSS spectra and stellar masses from the MPA-JHU catalog (Maddox et al. 2015). We note that the small Early Science (ES) sample from the MeerKAT International GigaHertz Tiered Extragalactic Exploration (MIGHTEE) survey also shows a median relation close to the relation for the ALFALFA galaxies (Maddox et al. 2021). The H I masses for most DLA/sub-DLAs with 21 cm detections (six out of eight) are higher than would be expected for their stellar masses based on the trend observed for the spectroscopic ALFALFA-SDSS sample, and higher than even the upper envelope of the latter trend. Such a trend could potentially result from a selection effect if the DLA/sub-DLA galaxies were somehow chosen to be more luminous than the ALFALFA galaxies, e.g., if the DLA/sub-DLA galaxies were systematically at higher redshifts than the ALFALFA galaxies. However, the redshift range $z < 0.08$ and the median redshift of 0.026 for the eight DLA/sub-DLA galaxies with H I masses and stellar masses shown in Figure 12 are roughly similar to those for the ALFALFA survey (which has a redshift range of $z < 0.06$ and a median redshift of ~ 0.03). Thus, observational selection cannot explain the higher brightness (in H I 21 cm emission) of the DLA/sub-DLA galaxies compared to the ALFALFA galaxies apparent from the upper panel of Figure 12.

Another possibility is that the detected 21 cm emission signal includes other bright galaxies in the field of view, given

that the FWHM of the GBT beam at 1.4 GHz is approximately 9.'3 in diameter. To assess this possibility, we searched for galaxies within a 9.'3 diameter region of the two GOTOQs with 21 cm emission detections, with similar g magnitude as our GOTOQ or brighter than that. For Q1457+531, there are two such galaxies: an early-type galaxy with no SDSS spectrum (but a photometric redshift of 0.135) 2.'77 away from the quasar and a late-type galaxy at $z = 0.0264$ separated by 4.'05 from the quasar. Given the large redshift differences in both cases from the redshift of our GOTOQ ($z_{gal} = 0.066$), both are unlikely to contribute much to the H I 21 cm emission detected with GBT. For Q1135+2414 ($z_{gal} = 0.0343$), there is a galaxy with no SDSS spectrum but a photometric redshift of 0.154 located 4.'9 away from the quasar. This galaxy also cannot contribute much to the GBT signal, both because its photometric redshift differs substantially from the redshift of our GOTOQ, and because it lies outside the FWHM of the GBT field of view. Thus, we conclude that our GBT 21 cm emission detections are associated with the corresponding GOTOQs, and that the corresponding estimates of H I masses of these galaxies should be robust. This suggests that low-z DLA/sub-DLA galaxies with H I and stellar mass determinations are intrinsically more gas-rich than typical local galaxies. Of course, given the small size of the current sample, it is essential to obtain H I 21 cm emission observations for many more DLA/sub-DLAs to examine whether the trends observed here also hold for the overall DLA/sub-DLA population. If confirmed with a larger sample, our findings would be consistent with the suggestion that absorption-selected galaxies are preferentially those with more extended gas disks and therefore have a larger gas reservoir (e.g., Klitsch et al. 2019). Those authors suggest that such conditions may arise due to galactic interactions, and that quasar absorbers may trace regions that are overdense in galaxies. Indeed, this suggestion is consistent with the large fraction of DLAs in our sample with multiple galaxies detected at the absorber redshift.

The lower panel of Figure 12 shows a plot of the ratio of H I mass to stellar mass versus the stellar mass for the DLA/sub-DLA galaxies and the corresponding trend for the spectroscopic ALFALFA-SDSS galaxies. The M_{HI}/M^* ratio flattens substantially at stellar masses below $\sim 10^9$ $M_\odot$ for the spectroscopic ALFALFA-SDSS sample. A flattening is not obvious for DLA/sub-DLA galaxies. Although the few absorption-based points do not conclusively show deviations from the main relation, such a trend, if present, would indicate that absorption-selected galaxies have larger gas reservoirs. Larger samples of DLA/sub-DLA galaxies (including those with high stellar masses) are essential to determine whether the M_{HI}/M^* ratio shows a flattening at any stellar mass for these galaxies. The flattening in M_{HI}/M^* observed for the ALFALFA-SDSS galaxies at $M^* \sim 10^9$ $M_\odot$ is believed to be connected to the fact that this stellar mass marks the transition between the hot- and cold-mode accretion in simulations at a baryonic mass of $\sim 2–3 \times 10^{10}$ $M_\odot$ (e.g., Kereš et al. 2009). The ALFALFA-SDSS galaxies with $M^* < 10^9$ $M_\odot$ are metal-poor and generally irregular in morphology, suggesting that their high H I fractions originate in recent gas accretion rather than inefficient star formation (Maddox et al. 2015). The possibility of even higher H I fractions for DLA/sub-DLA galaxies, together with their high sSFRs seen at $M^* < 10^9$ $M_\odot$ (see Figure 10), suggest that DLA/sub-DLA galaxies may also have undergone recent gas accretion. It will be very interesting
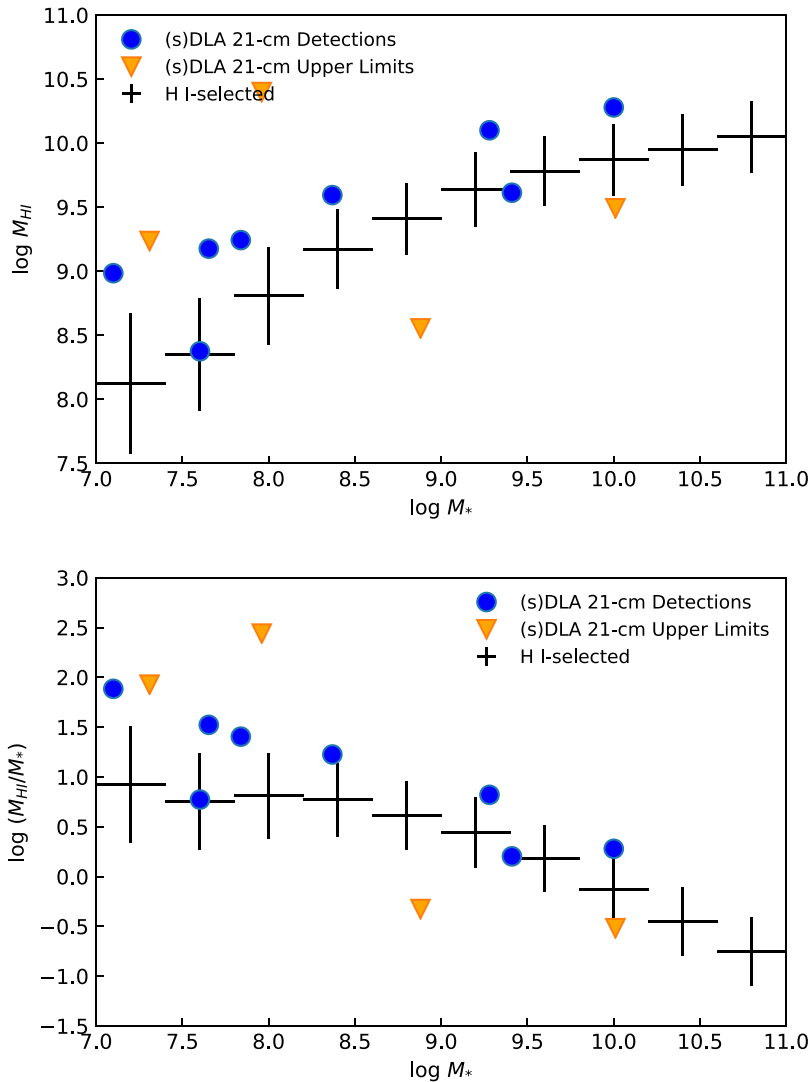
Figure 12. Top (a): H I gas mass vs. stellar mass for galaxies associated with DLAs searched for in 21 cm emission from our sample and the literature. Bottom (b): ratio of H I gas mass to stellar mass, plotted vs. stellar mass for galaxies associated with DLAs searched for in 21 cm emission from our sample and the literature. Also shown in both panels are the corresponding relations (median values and $\pm 1\sigma$ uncertainties) deduced for galaxies selected by H I emission, based on 9,153 ALFALFA galaxies with SDSS spectra and stellar masses (Maddox et al. 2015). See the text for more details.

to obtain higher-resolution UV spectra in the future to determine the metallicities of these DLA/sub-DLAs and assess whether they are consistent with the recent accretion scenario (low metallicities would be expected if the gas is recently accreted). We also note that the currently available MIGHTEE ES sample is much smaller (~300 galaxies with $0 < z < 0.084$) than the ALFALFA-SDSS sample. Once the full MIGHTEE survey is completed providing a much larger galaxy sample spanning $0 < z < 0.6$, it will be very interesting to examine the median H I mass versus stellar mass trend and the redshift evolution in this trend for that large sample, and to compare DLA/sub-DLA galaxies with detections of H I 21 cm emission against these trends.

In view of our finding in Section 5.5.1 that the H I column density appears to be anticorrelated with stellar mass, it is also interesting to examine how the H I column density correlates with the H I mass. For this purpose, we considered the eight cases with H I 21 cm detections, of which seven absorbers have N_{HI} measurements based on the Lyα absorption line. This small sample shows a Spearman rank order correlation coefficient of -0.252 between N_{HI} and M_{HI}, which is not

significant at the <0.05 level of probability. Of course, a larger sample of objects with H I 21 cm emission and Lyα absorption measurements is needed to search more meaningfully for any trend.

We also note that the logarithmic H I to stellar mass ratios for the Leo P and Leo T dwarf galaxies are ≈ 0.25 and ≈ 0.4, respectively. The flattening of the M_{HI}/M^* ratio at low stellar masses has been suggested as an evidence that dark galaxies (which are rich in H I but low in stellar mass) are not a substantial population (Maddox et al. 2015). The lack of flattening in M_{HI}/M^* seen for DLA/sub-DLAs, if confirmed with a larger sample, would raise questions about this interpretation, especially if the rise in M_{HI}/M^* continues to even lower stellar masses. Expanding optical and radio studies of DLAs/sub-DLAs may thus have important implications for dark galaxies.

5.5.7. Is the Absorbing Gas Bound to the Galaxies?

It is of interest to understand whether or not the cool H I gas detected in DLA/sub-DLAs is bound to the galaxies. To
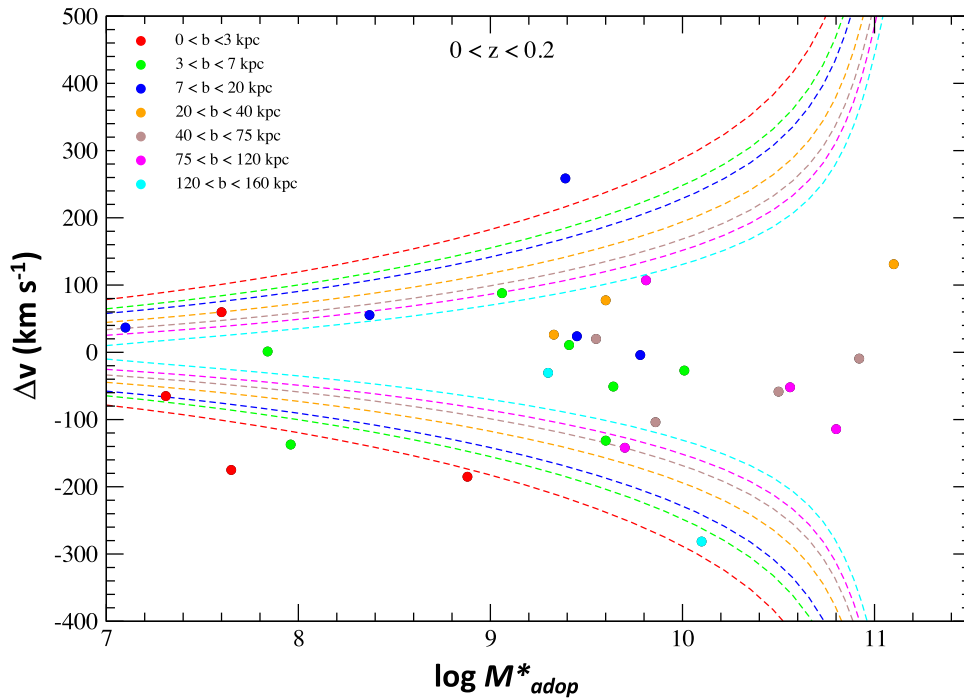
Figure 13. Velocity offsets of DLA/sub-DLA absorbers with respect to the galactic systemic redshifts, compared to the expected escape velocities in the galaxies. Colored points show the DLA/sub-DLAs at $0 < z < 0.2$ in our sample, separated by impact parameters. The red, green, blue, orange, brown, magenta, and cyan dashed curves show, respectively, the expected escape velocities at distances of 1, 5, 10, 30, 60, 90, and 140 kpc from the centers of galaxies at $z = 0.1$. See the text for more details.

examine this, we compare the velocity offsets of the absorbers relative to the systemic redshifts of the galaxies with the expected escape velocities at the impact parameters of the quasar sight lines. To estimate the escape velocity at a distance r from the galaxy center, we use the relation

$$v_{\rm esc} = v_{cir}(2[1 + \ln(r_{\rm max}/r)])^{1/2} , \qquad (4)$$

assuming the dark matter halo to be an isothermal sphere truncated at radius $r_{\rm max}$ (Heckman et al. 2000). For the circular velocity v_{cir}, we adopt the relation

$$v_{\rm cir} = (GM_h/r_h)^{1/2}, \qquad (5)$$

where M_h and r_h are the halo mass and halo radius, respectively (Mo & White 2002). We approximate $r_{\rm max}$ as the halo radius r_h (Xu et al. 2021), given by

$$r_h = (GM_h/100\Omega_m H_0^2)^{1/3}(1 + z)^{-1}. \qquad (6)$$

For the relation between the halo mass and the stellar mass, we adopt the recent parameterization mentioned earlier (Girelli et al. 2020). Figure 13 shows the velocity offsets of the DLA/sub-DLA absorbers with respect to the galaxies for the galaxies at $z < 0.2$ in our sample. The dashed curves show the escape velocity at distances of 1, 5, 10, 30, 60, 90, and 140 kpc from the galaxy centers. For most of the galaxies, the velocity offsets are less than the escape velocity, indicating that the absorbing gas in these galaxies is gravitationally bound to the galaxies. There are a few galaxies, for which the velocity offset exceeds the escape velocity at the corresponding distance; these DLA/sub-DLAs may be associated with unbound outflows. The majority of DLA/sub-DLAs at $z < 0.2$, however, appear to not have significant outflows. This conclusion is similar to recent results for low-redshift Mg II absorbers (e.g., Huang et al. 2021). We caution, however, that our absorption line

measurements are based on the H I Lyα profiles measured in the low-resolution COS G140L spectra. Considering that there is a velocity spread in absorption along each line of sight, it would be necessary to examine the full range of velocities in each individual absorber to understand whether all of the gas is bound or whether gas at some velocities could correspond to unbound outflows. As stated in Section 5.5.3, it will be interesting to determine the gas kinematics more accurately using higher-resolution spectroscopy of the background quasar and integral field spectroscopy of the foreground galaxy.

6. Conclusions

We have targeted 10 quasars selected from our GOTOQs sample with HST/COS in order to study the H I characteristics of the galactic disks. Eight of these sight lines had sufficient quasar flux at the wavelengths of interest, and all eight of these showed strong H I absorption: seven DLAs and one sub-DLA. Thus, we have a 100% detection rate of DLA or sub-DLA systems in the disks of low−z galaxies. Indeed, this is the largest systematically targeted sample of DLAs associated with low-redshift galaxies. Additionally, our low-resolution COS spectra provide approximate measurements of metal absorption lines and their equivalent widths. A search for H I 21 cm emission measurements for five of the fields led to two detections and three nondetections.

Combining our sample with the literature, we obtained a sample of 117 galaxies associated with DLAs/sub-DLAs and examined the correlations between different galaxy and absorber properties. While this includes both galaxy-selected and absorber-selected samples, the combined sample allows us to examine basic scaling relations between galaxy and absorber properties, and reveals a number of interesting trends:

(1) The SFR correlates positively with redshift overall, with a strong rise at lower redshifts and a possible flattening at $z \gtrsim 2$. It would be interesting to expand the high-z sample to determine the SFH of DLA/sub-DLA galaxies more accurately.

(2) The H I column density is inversely correlated with the impact parameter, consistent with past findings based on smaller samples. Our sample shows that this trend appears to extend even to the smallest impact parameters probed ($\lesssim 1$ kpc). This confirms the general expectation that the probability of a random sight line to a background quasar passing through a region gas-rich enough to be detectable as a DLA/sub-DLA decreases with increasing galactocentric distance.

(3) The H I column density is inversely correlated with the stellar mass, in agreement with past findings based on smaller samples. This trend is also consistent with past suggestions that sub-DLAs may arise in more massive galaxies than DLAs. These results are consistent with past findings that a large fraction of the DLA cross section arises in sub-L^* galaxies.

(4) Roughly equal incidences of positive and negative velocity offsets are observed between the absorbers and the galaxies. A combination of high-resolution spectroscopy and integral field spectroscopy is needed to determine the origins of the gas in individual cases.

(5) A positive correlation is observed between the stellar mass and the impact parameter, possibly indicating that more massive galaxies can have gas-rich regions detectable as DLA/sub-DLAs out to larger galactocentric distances, i.e., their deeper gravitational potential wells may allow them to hold on to neutral gas extending farther away from the center. The larger masses could potentially result from more pronounced galactic interactions, in line with recent suggestions that quasar absorbers preferentially trace more overdense regions.

(6) A substantial fraction of DLA/sub-DLA galaxies with independent estimates of stellar mass and SFR and/or stellar mass and luminosity appear to be generally consistent with the SFR versus M^* and luminosity versus M^* trends for star-forming galaxies.

(7) The sSFR shows a positive correlation with redshift and a negative correlation with stellar mass. However, while the sSFRs for most DLA/sub-DLA galaxies are broadly consistent with the expectations from the SFMS for star-forming galaxies, a significant fraction of the DLA/sub-DLA galaxies ($\sim$20%) lies below the SFMS. This illustrates how studies of DLA/sub-DLAs can complement studies of galactic evolution and extend them to lower stellar masses and lower SFRs.

(8) Indeed, the relevance of DLA/sub-DLAs for the study of gas-rich galaxies is also evident from the higher H I mass to stellar mass ratio for most DLA/sub-DLA galaxies with detections of H I 21 cm emission compared to local spiral and irregular galaxies, and even relative to the H I emission-selected ALFALFA-SDSS galaxies. The high M_{HI}/M^* ratio and high sSFRs seen in DLA/sub-DLA galaxies with $M^* < 10^9 M_\odot$ suggest that these galaxies may be gas-rich because of recent gas accretion rather than inefficient star formation.

(9) The H I gas in most of the DLA/sub-DLAs at $z < 0.2$ appears to be gravitationally bound to the galaxies. Higher-resolution spectroscopy of the background quasar is essential to determine the kinematics of the absorbing gas more accurately.

To make further progress on the nature of the gas flows around these galaxies, it is imperative to determine the metallicity of the absorbing gas. Follow-up higher-resolution and shorter-wavelength UV spectra are essential to more accurately measure the column densities of the metal lines, and to cover higher Lyman series lines. Absorption-line metallicities obtained from future higher-resolution HST spectroscopic studies can be compared with metallicities of the galaxies based on nebular emission lines to estimate the metallicity gradients in the galaxies. It is also essential to estimate H I masses of galaxies using radio interferometers to overcome the potential for confusion that can affect single dish H I 21 cm measurements. The ongoing large H I 21 cm emission line surveys such as MALS (Gupta et al. 2016) and WALLABY (Koribalski et al. 2020) with the Square Kilometre Array precursor telescopes will deliver such samples of nearby galaxies to understand the origin of gas producing DLA/sub-DLAs.

The metallicities and dust contents of GOTOQs inferred from future studies can be combined with the remaining properties discussed in this paper for determination of the mass–metallicity relation (MZR) of the low-z DLA/sub-DLAs, and to assess how the MZR has been evolving with redshift for the absorbing galaxies. The metallicities will also help to better understand whether the DLA/sub-DLAs with H I 21 cm detections indeed experienced recent accretion of metal-poor gas. Rest-frame UV and optical continuum imaging of more DLA/sub-DLAs is essential to increase the sample with luminosity measurements that can be combined with the stellar mass measurements to investigate the mass-to-light ratios of the absorbing galaxies. Also necessary are optical spectra of the galaxies to determine their total flux profile, and high-resolution HST imaging to ascertain the exact morphological profiles of these galaxies. Follow-up high-resolution spectroscopy of the background quasars, combined with integral field spectroscopy of the galaxies, would also be instrumental in determining the kinematics of the cool gas and warm ionized gas in these galaxies.

Finally, it is also important to fill in the large gaps in redshift space seen in Figures 9 and 10(a), especially at $1 \lesssim z \lesssim 2$. This along with an increase in the existing number of galaxies associated with DLAs and sub-DLAs at $z < 1$ and $z > 2$ is essential in order to build a more comprehensive picture of the evolution of the DLA and sub-DLA populations and to better understand their overall significance in studies of galactic evolution (for example, to better understand the physics involved in the transformation of the cold gas into stars in galaxies). Our work demonstrates that absorption studies of DLA/sub-DLAs combined with emission studies of the galaxies producing them have the power to probe regimes of low stellar mass and low SFR that are not sampled well with current flux-limited galaxy surveys.

ORCID iDs

Varsha P. Kulkarni ● https://orcid.org/0000-0002-2587-2847
David V. Bowen ● https://orcid.org/0000-0002-5668-0397
Lorrie A. Straka ● https://orcid.org/0000-0001-5892-6760
Neeraj Gupta ● https://orcid.org/0000-0001-7547-4241
Pasquier Noterdaeme ● https://orcid.org/0000-0002-5777-1629

References

Augustin, R., Péroux, C., Moller, P., et al. 2018, MNRAS, 478, 3120
Battisti, A. J., Meiring, J. D., Tripp, T. M., et al. 2012, ApJ, 744, 93
Bergeron, J., & Boisse, P. 1991, A&A, 234, 344
Bohlin, R. C., Savage, B. D., & Drake, J. F. 1978, ApJ, 224, 132
Boissier, S., Péroux, C., & Pettini, M. 2003, MNRAS, 338, 131
Bolzonella, M., Miralles, J.-M., & Pelló, R. 2000, A&A, 363, 476
Boogaard, L. A., Brinchmann, J., Bouché, N., et al. 2018, A&A, 619, A27
Borthakur, S., Momjian, E., Heckman, T. M., et al. 2019, ApJ, 871, 239
Borthakur, S., Tripp, T. M., Yun, M. S., et al. 2010, ApJ, 713, 131
Bothwell, M. S., Wagg, J., Cicone, C., et al. 2014, MNRAS, 445, 2599
Bowen, D. V., Chelouche, D., Jenkins, E. B., et al. 2016, ApJ, 826, 50
Bowen, D. V., Jenkins, E. B., Pettini, M., & Tripp, T. M. 2005, ApJ, 635, 880
Bowen, D. V., Jenkins, E. B., Tripp, T. M., et al. 2008, ApJS, 176, 59
Bruzual, G., & Charlot, S. 2003, MNRAS, 344, 1000
Calette, A. R., Avila-Reese, V., Rodriguez-Puebla, A., Hernandez-Toledo, H., & Papastergis, E. 2018, RMxAA, 54, 443
Carilli, C., & van Gorkom, J. 1992, ApJ, 399, 373
Cen, R. 2012, ApJ, 748, 121
Christensen, L., Moller, P., Fynbo, J. P. U., & Zafar, T. 2014, MNRAS, 445, 225
Christensen, L., Noterdaeme, P., Petitjean, P., Ledoux, C., & Fynbo, J. P. U. 2009, A&A, 505, 1007
Christensen, L., Schulte-Ladbeck, R., Sanchez, S. F., et al. 2005, A&A, 429, 477
Cimatti, A., Fraternali, F., & Nipoti, C. 2020, Introduction to Galaxy Formation and Evolution: From Primordial Gas to Present-day Galaxies (Cambridge: Cambridge Univ. Press)
Cooke, R., Pettini, M., & Joregenson, R. A. 2015, ApJ, 800, 12
Dey, A., Schlegel, D. J., Lang, D., et al. 2019, AJ, 157, 168
Djorgovski, S. G., Pahre, M. A., Bechtold, J., & Elston, R. 1996, Natur, 382, 234
Dupuis, C. M., Borthakur, S., Padave, M., et al. 2021, ApJ, 907, 103
Dutta, R., Srianand, R., Gupta, N., et al. 2017a, MNRAS, 465, 588
Ford, A. B., Oppenheimer, B. D., Davé, R., et al. 2013, MNRAS, 432, 89
Frye, B. L., Bowen, D. V., Tripp, T. M., et al. 2019, ApJ, 872, 129
Fynbo, J. P. U., Geier, S. J., Christensen, L., et al. 2013, MNRAS, 436, 361
Girelli, G., Pozzetti, L., Bolzonella, M., et al. 2020, A&A, 634, 135
Gupta, N., Srianand, R., Bowen, D. V., York, D. G., & Wadadekar, Y. 2010, MNRAS, 408, 849
Gupta, N., Srianand, R., Farnes, J. S., et al. 2018, MNRAS, 476, 2432
Gupta, N., Srianand, R., Noterdaeme, P., Petitjean, P., & Muzahid, S. 2013, A&A, 558, 84
Gupta, N., Srianand, R., Petitjean, P., et al. 2012, A&A, 544, A21
Gupta, N., Srianand, R., Baan, W., et al. 2016, Proc. of MeerKAT Science: On the Pathway to the SKA (Trieste: SISSA), 14
Hamanowicz, A., Péroux, C., Zwaan, M. A., et al. 2020, MNRAS, 492, 2347
Hayes, M., Östlin, G., Mas-Hesse, J. M., et al. 2005, A&A, 438, 71
Heckman, T. M., Lehnert, M. D., Strickland, D. K., & Lee, A. 2000, ApJS, 129, 493
Huang, Y.-H., Chen, H.-W., Shectman, S. A., et al. 2021, MNRAS, 502, 4743
Jimenez, R., Bowen, D. V., & Matteucci, F. 1999, ApJL, 514, L83
Joshi, R., Fumagalli, M., Srianand, R., et al. 2021, ApJ, 908, 129
Joshi, R., Srianand, R., Noterdaeme, P., & Petitjean, P. 2017, MNRAS, 465, 701
Joshi, R., Srianand, R., Noterdaeme, P., & Petitjean, P. 2017, MNRAS, 471, 1910
Kacprzak, G., Murphy, M. T., & Churchill, C. W. 2010, MNRAS, 406, 445
Kanekar, N., Neeleman, M., Prochaska, J. X., & Ghosh, T. 2018, MNRAS, 473, L54
Kanekar, N., Prochaska, J. X., Neeleman, M., et al. 2020, ApJL, 901, L5
Kaur, B., Kanekar, N., Rafelski, M., et al. 2021, ApJ, 921, 68
Kennicutt, R. C. 1992, ApJ, 388, 310
Kennicutt, R. C. 1998, ARA&A, 36, 189
Kereš, D., Katz, N., Fardal, M., Davé, R., & Weinberg, D. H. 2009, MNRAS, 395, 160
Khare, P., Kulkarni, V. P., Péroux, C., et al. 2007, A&A, 464, 487
Klitsch, A., Zwaan, M. A., Péroux, C., et al. 2019, MNRAS, 482, L65
Koribalski, B. S., Staveley-Smith, L., Westmeier, T., et al. 2020, Ap&SS, 365, 118
Krogager, J.-K., Møller, P., Christensen, L. B., et al. 2020, MNRAS, 495, 3014
Krogager, J.-K., Møller, P., Fynbo, J. P. U., & Noterdaeme, P. 2017, MNRAS, 469, 2959
Kulkarni, V. P., Fall, S. M., Lauoresch, J. T., et al. 2005, ApJ, 618, 68
Kulkarni, V. P., Hill, J. M., Schneider, G., et al. 2000, ApJ, 536, 36
Kulkarni, V. P., Hill, J. M., Schneider, G., et al. 2001, ApJ, 551, 37
Kulkarni, V. P., Khare, P., Som, D., et al. 2010, NewA, 15, 735
Kulkarni, V. P., Meiring, J., Som, D., et al. 2012, ApJ, 749, 176
Kulkarni, V. P., Som, D., Morrison, S., et al. 2015, ApJ, 815, 24
Kulkarni, V. P., Woodgate, B. E., York, D. G., et al. 2006, ApJ, 636, 30
Kunth, D., Leitherer, C., Mas-Hesse, J. M., Östlin, G., & Petrosian, A. 2003, ApJ, 597, 263
Le Brun, V., Bergeron, J., Boissé, P., & Deharveng, J. M. 1997, A&A, 321, 733
Ledoux, C., Noterdaeme, P., Petitjean, P., & Srianand, R. 2015, A&A, 580, A8
Leroy, A. K., Walter, F., Brinks, E., et al. 2008, AJ, 136, 2782
Lizst, H. 2014, ApJ, 780, 10
Ma, J., Brammer, G., Ge, J., Prochaska, J. X., & Lundgren, B. 2018, ApJL, 857, L12
Mackenzie, R., Fumagalli, M., Theuns, T., et al. 2019, MNRAS, 487, 5070
Madau, P., & Dickinson, M. 2014, ARAA, 52, 415
Maddox, N., Frank, B. S., Ponomareva, A. A., et al. 2021, A&A, 646, A35
Maddox, N., Hess, K. M., Obreschkow, D., Jarvis, M. J., & Blyth, S.-L. 2015, MNRAS, 447, 1610
McGaugh, S. S. 2012, AJ, 143, 40
Mitchell, P. D., Lacey, C. G., Baugh, C. M., & Cole, S. 2016, MNRAS, 456, 1459
Mo, H. J., & White, S. D. M. 2002, MNRAS, 336, 112
Møller, P., Warren, S. J., Fall, S. M., Fynbo, J. U., & Jakobsen, P. 2002, ApJ, 574, 51
Moustakas, J., Kennicutt, R. C., & Tremonti, C. 2006, ApJ, 642, 775
Neeleman, M., Kanekar, N., Prochaska, J. X., et al. 2017, Sci, 355, 1285
Neeleman, M., Kanekar, N., Prochaska, J. X., Rafelski, M. A., & Carilli, C. L. 2019, ApJL, 870, L19
Neeleman, M., Prochaska, J. X., Kanekar, N., & Rafelski, M. 2020, Natur, 581, 269
Nelson, D., Sharma, P., Pillepich, A., et al. 2020, MNRAS, 498, 2391
Nielsen, N. M., Churchill, C. W., & Kacprzak, G. G. 2013, ApJ, 776, 115
Noterdaeme, P., Laursen, P., Petitjean, P., et al. 2012a, A&A, 540, A63
Noterdaeme, P., Petitjean, P., Ledoux, C., & Srianand, R. 2009, A&A, 505, 1087
Noterdaeme, P., Petitjean, P., Carithers, W. C., et al. 2012b, A&A, 547, L1
Noterdaeme, P., Petitjean, P., Pâris, I., et al. 2014, A&A, 566, A24
Noterdaeme, P., Srianand, R., & Mohan, V. 2010, MNRAS, 403, 906
Oke, J. B., & Gunn, J. E. 1983, ApJ, 266, 713
Östlin, G., Hayes, M., Kunth, D., et al. 2009, AJ, 138, 923
Péroux, C., Bouché, N., Kulkarni, V. P., York, D. G., & Vladilo, G. 2011, MNRAS, 410, 2237

Péroux, C., Dessauges-Zavadsky, M., D'Odorico, S., Kim, T.-S., & McMahon, R. G. 2005, MNRAS, 363, 479
Péroux, C., Dessauges-Zavadsky, M., D'Odorico, S., Kim, T.-S., & McMahon, R. G. 2007, MNRAS, 382, 177
Péroux, C., Kulkarni, V. P., & York, D. G. 2014, MNRAS, 437, 3144
Péroux, C., Quiret, S., Rahmani, H., et al. 2016, MNRAS, 457, 903
Péroux, C., Rahmani, H., Quiret, S., et al. 2017, MNRAS, 464, 2053
Péroux, C., Zwaan, M. A., Klitsch, A., et al. 2019, MNRAS, 485, 1595
Pettini, M. 2011, RSPSA, 467, 2735
Pettini, M., Smith, L. J., King, D. L., & Hunstead, R. W. 1997, ApJ, 486, 665
Pontzen, A., Governato, F., Pettini, M., et al. 2008, MNRAS, 390, 1349
Popping, G., Somerville, R. S., & Trager, S. C. 2014, MNRAS, 442, 2398
Prochaska, J. X., Herbert-Fort, S., & Wolfe, A. M. 2005, ApJ, 635, 123
Prochaska, J. X., & Wolfe, A. M. 2009, ApJ, 696, 1543
Quiret, S., Péroux, C., Zafar, T., et al. 2016, MNRAS, 458, 4074
Rafelski, M., Wolfe, A. M., & Chen, H.-W. 2011, ApJ, 736, 48
Rafelski, M., Wolfe, A. M., Prochaska, J. X., Neeleman, M., & Mendez, A. J. 2012, ApJ, 755, 89
Rahmani, H., Péroux, C., Augustin, R., et al. 2018, MNRAS, 474, 254
Rahmati, A., & Schaye, J. 2014, MNRAS, 438, 529
Ranjan, A., Noterdaeme, P., Krogager, J.-K., et al. 2020, A&A, 633, 125
Rao, S. M., Nestor, D. B., Turnshek, D. A., et al. 2003, ApJ, 595, 94
Rhodin, N. H. P., Christensen, L., Moller, P., Zafar, T., & Fynbo, J. P. U. 2018, A&A, 618, 129
Rhodin, N. H. P., Krogager, J.-K., Christensen, L., et al. 2021, MNRAS, 506, 546
Rosenberg, J. L., Bowen, D. V., Tripp, T. M., & Brinks, E. 2006, AJ, 132, 478
Savage, B. D., Drake, J. F., Budich, W., & Bohlin, R. C. 1977, ApJ, 216, 291
Sembach, K. R., & Savage, B. D. 1992, ApJS, 83, 147
Som, D., Kulkarni, V. P., Meiring, J., et al. 2015, ApJ, 806, 25

Srianand, R., Hussain, T., Noterdaeme, P., et al. 2016, MNRAS, 460, 634
Straka, L. A., Kulkarni, V. P., & York, D. G. 2011, AJ, 141, 206
Straka, L. A., Kulkarni, V. P., York, D. G., Woodgate, B. E., & Grady, C. A. 2010, AJ, 139, 1144
Straka, L. A., Noterdaeme, P., Srianand, R., et al. 2015, MNRAS, 447, 3856
Straka, L. A., Whichard, Z. L., Kulkarni, V. P., et al. 2013, MNRAS, 436, 3200
Szakacs, R., Péroux, C., Zwaan, M., et al. 2021, MNRAS, 505, 4746
Thorne, J. E., Robotham, A. S. G., Davies, L. J. M., et al. 2021, MNRAS, 505, 540
van de Voort, F., Schaye, J., Altay, G., & Theuns, T. 2012, MNRAS, 421, 2809
Viegas, S. M. 1995, MNRAS, 276, 268
Vladilo, G., Centurión, M., Bonifacio, P., & Howk, J. C. 2001, ApJ, 557, 1007
Werk, J., Prochaska, J. X., Tumlinson, J., et al. 2014, ApJ, 792, 8
Whitaker, K. E., Franx, M., Leja, J., et al. 2014, ApJ, 795, 104
Whitaker, K. E., Franx, M., Leja, J., et al. 2020, ApJ, 896, 175
Wisotzki, L., Bacon, R., Blaizot, J., et al. 2016, A&A, 587, 98
Wolfe, A. M., Turnshek, D. A., Smith, H. E., & Cohen, R. D. 1986, ApJS, 61, 249
Xu, Y., Ouchi, M., Rauch, M., et al. 2021, ApJ, in press, arXiv:2112.08045
York, D. G., Lundgren, B., et al. 2022, to be submitted
York, D. G., Adelman, J., Anderson, J. E., Jr., et al. 2000, AJ, 120, 1579
York, D. G., Dopita, M., & Green, R. 1986, ApJ, 311, 610
York, D. G., Straka, L. A., Bishof, M., et al. 2012, MNRAS, 423, 3692
Zafar, T., Centurion, M., Molaro, P., et al. 2014, MmSAI, 85, 363
Zafar, T., Møller, P., Péroux, C., et al. 2017, MNRAS, 465, 1613
Zafar, T., Péroux, C., Popping, A., et al. 2013, A&A, 556, A141
Zwaan, M., Walter, F., Ryan-Weber, E., et al. 2008, AJ, 136, 2886
Zwaan, M. A., van der Hulst, J. M., Briggs, F. H., Verheijen, M. A. W., & Ryan-Weber, E. V. 2005, MNRAS, 364, 1467